Final Scientific/Technical Report
Date of Report: July 6, 2016

Award Number: DE-EE0005665

Project Title: Roots Air Management System with Integrated Expander

Project Period: July 5, 2012 – June 30, 2016

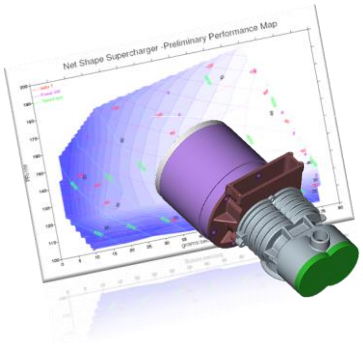

Recipient Organization: Eaton
W126N7250 Flint Drive
Menomonee Falls, WI 53051-4404
DUNS: 360921261

Technical Contact: Dale Stretch
E-mail: DaleAStretch@eaton.com
Phone: (248) 226-6799

Co-Principal Investigator Roots Expander Development Phase: William N. Eybergen
E-mail: BillNEybergen@eaton.com
Phone: (248) 226-6998

Contractual Contact: Cindy K. Shane, Manager Government Contracts
Eaton
E-mail: Lucindakshane@eaton.com
Phone: (414) 449-6607

Partners: Ballard Power Systems
Kettering University
Electricore, Inc.

Report Submitted For: Energy Efficiency & Renewable Energy (EERE) DOE / National Energy Technology Laboratory (NETL)

DOE Project Officer: Gregory J. Kleen
E-mail: gregory.kleen@ee.doe.gov
Phone: 240-562-1672

DOE Contract Specialist: Carlo DiFranco
E-mail: carlo.difranco@go.doe.gov
Phone: 720-356-1316

Acknowledgment: This material is based upon work supported by the Department of Energy under Award Number DE-EE0005665.

Contents

LIST OF TABLES

LIST OF FIGURES

1 EXECUTIVE SUMMARY

PEM fuel cells remain an emerging technology in the vehicle market with several cost and reliability challenges that must be overcome in order to increase market penetration and acceptance. The DOE has identified the lack of a cost effective, reliable, and efficient air supply system that meets the operational requirements of a pressurized PEM 80kW fuel cell as one of the major technological barriers that must be overcome. This project leveraged Roots positive displacement development advancements and demonstrated an efficient and low cost fuel cell air management system. Eaton built upon its P-Series Roots positive displacement design and shifted the peak efficiency making it ideal for use on an 80kW PEM stack. Advantages to this solution include:

- Lower speed of the Roots device eliminates complex air bearings present on other systems.
- Broad efficiency map of Roots based systems provides an overall higher drive cycle fuel economy.
- Core Roots technology has been developed and validated for other transportation applications.

Eaton modified their novel R340 Twin Vortices Series (TVS) Roots-type supercharger for this application. The TVS delivers more power and better fuel economy in a smaller package as compared to other supercharger technologies. By properly matching the helix angle with the rotor's physical aspect ratio, the supercharger's peak efficiency can be moved to the operating range where it is most beneficial for the application. The compressor was designed to meet the 90 g/s flow at a pressure ratio of 2.5, similar in design to the P-Series 340. A net shape plastic expander housing with integrated motor and compressor was developed to significantly reduce the cost of the system. This integrated design reduced part count by incorporating an overhung expander and motor rotors into the design such that only four bearings and two shafts were utilized.

2 ACCOMPLISHMENTS

Specific project objectives include:

Primary Objectives

- 62/64% (baseline 2011) > 65/70% (target 2017) Compressor/expander efficiency at 25% of full flow
- 80% (baseline 2011) > 90% (target 2017) Combined motor/motor controller efficiency at full flow
- 11.0/17.3kW (baseline2011) < 8/14kW (target 2017) Compressor/expander input power at 100% of full flow

Secondary Objectives

- Meeting all 2017 Project Target objectives in Table 1
- Conduct a cost reduction analysis to identify areas for additional possible cost reductions

A fully tested and validated TRL 7 Air Management System hardware capable of meeting the 2017 Project Targets in Table 1 was delivered at the conclusion of this project.

Table 1 below displays a tabulated comparison of key performance parameters for Eaton's actual performance versus original project and DOE goals.

Table 1: 2017 Project Targets

Characteristic	Units	Eaton Status	DOE Target 2017	Project Target 2015
Input power[a] at full flow[b], (with expander / without expander)	kW_e	10.6 / 14.8	8 / 14	8 / 14
Combined motor & motor controller efficiency at full flow[b]	%	93	90	90
Compressor / expander efficiency at full flow (C/E only)[b]	%	65 / 65	75 / 80	75 / 75
Input power at 25% flow[c] (with expander/without expander)	kW_e	2.0/2.0	1.0 / 2.0	1.0 / 2.0
Combined motor & motor controller efficiency at 25% flow[c]	%	82	80	80
Compressor / expander efficiency at 25% flow[c]	%	65 / 51	65 / 70	65 / 70
Input power at idle[d] (with / without expander)	W_e	405 / 405	200 / 200	200 / 200
Combined motor / motor controller efficiency at idle[d]	%	50	70	---
Compressor / expander efficiency at idle[d]	%	21	60 / 60	60 / 60
Turndown ratio (max/min flow rate)		20	20	20
Noise at maximum flow (excluding air flow noise at air inlet and exhaust)	dB(A) at 1 meter	65 (with enclosure & suppression)	65	65 (with enclosure & suppression)
Transient time for 10 - 90% of maximum airflow	sec	1	1	1
System volume[e]	liters	10.8	15	15
System weight[e]	kg	15.9	15	15
System cost[f]	$	984	500	500
Input power[a] at full flow[b], (with expander / without expander)	kW_e	10.6 / 14.8	8 / 14	8 / 14

[a] Electrical input power to motor controller when bench testing fully integrated system. Fully integrated system includes control system electronics, air filter, and any additional air flow that may be used for cooling.
[b] Compressor: 92 g/s flow rate, 2.5 bar (absolute) discharge pressure; 40°C, 25% RH inlet conditions. Expander: 88 g/s flow rate, 2.2 bar (absolute) inlet pressure, 70°C, 100% RH inlet conditions.
[c] Compressor: 23 g/s flow rate, minimum 1.5 bar (absolute) discharge pressure; 40°C, 25% RH inlet conditions. Expander: 23 g/s flow rate, 1.4 bar (absolute) inlet pressure, 70°C, 100% RH inlet conditions.
[d] Compressor: 4.6 g/s flow rate, minimum 1.2 bar (absolute) discharge pressure; 40°C, 25% RH inlet conditions. Expander: 4.6 g/s flow rate, < compressor discharge pressure, 70°C, 20% RH inlet conditions.
[e] Weight and volume include the motor, motor controller and system enclosure.
[f] Cost target based on a manufacturing volume of 500,000 units per year.
[g] DTI cost model of the Honeywell 100,000 rpm machine, 2.5 bar (absolute), 92 g/s, dry air, 40°C: $960 including markup. TIAX 2009 estimate of Honeywell technology (compressor, expander, motor, motor controller) presented at 2010 Annual Merit Review and Peer Evaluation: $790 including 15% markup.

3 PROJECT ACTIVITY SUMMARY

3.1 Analytical Development of the Compressor & Expander using CFD Modeling

Eaton's CFD software of choice used to evaluate the efficiency of positive displacement Roots device was not able to converge the analysis due to the small clearances between the rotor tips and housing wall. To overcome this limitation, the clearances were increased approximately three times from the targeted design values to allow for the model to successfully run, see Figure 1. The increased clearance impacts the device volumetric efficiency and requires a correction to the RPM to match the targeted flow. To validate the impact, efficiency tests were run the baseline design in supercharger and expander flow directions. The data showed that there was approximately a 10% reduction in efficiency with the increased clearance which correlation to the CFD analysis results as per Figure 2 & Figure 3. Upon validation, the CFD model was then used to develop the expander inlet and outlet designs.

Internal Eaton resources completed the initial CFD modeling as Kettering University developed an alternative CFD approach with a different software package to enable for the desired clearances to be evaluated.

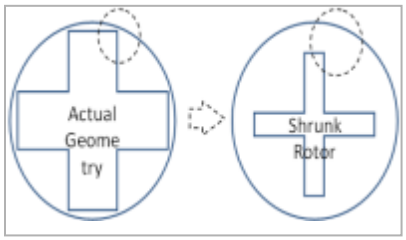

Figure 1: Limitation of FLUENT capabilities overcome by scaling clearance to 600 micron

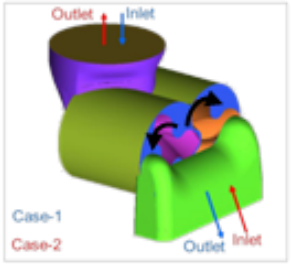

Figure 2: Design 1 expander tested for reverse and forward flow showed a 10 % decrease in efficiency

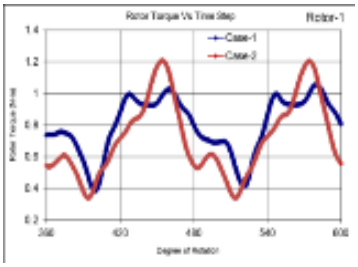

Figure 3: Modeling of expander also predicted a 10% decrease in efficiency

3.1.1 *New CFD Tool Approach and Development Background*

Kettering's first step was to access several CFD, grid-generation, and post-processing software tools. Due to the complexity of the Roots rotor geometries and small clearances that exist between the rotors components, the first software tool used to generate the FEA grid contained numerous distorted and skewed cells. Several attempts were made to eliminate these distorted cells, but STAR-CCM+ mesh was never successful.

As a result, a decision was made to use a more specialized grid-generation software. This tool had a better meshing algorithm and was able to generate an accurate grid as outlined Figures 4 and 5. This meshing process was very labor intensive since the geometry does not contain any axis-symmetry that could have simplified the meshing process. Figures 6 and 7 show the interior mesh in two cut planes, one along the axis of the rotors, and one perpendicular to the axis. The small clearances that exist between the rotors and the housing are clearly visible in these figures. Figures 8 and 9 show the refined mesh created around each rotor. These regions are required in order to accurately model each rotor. The analysis successfully completed three revolutions of the rotors.

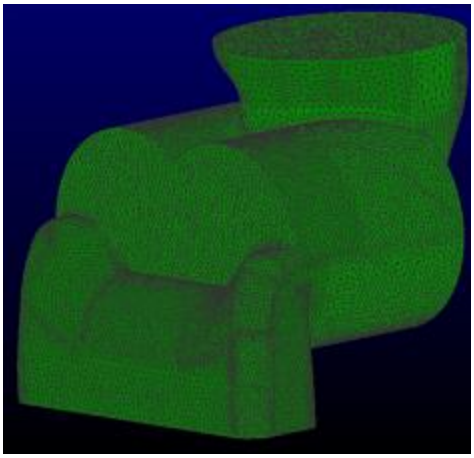

Figure 4: Mesh of the expander

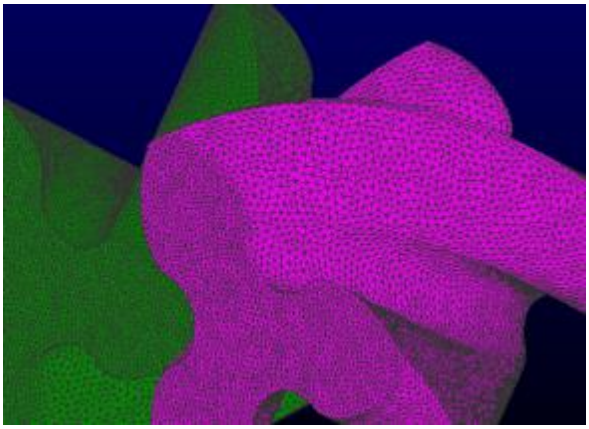

Figure 5: Meshed rotors

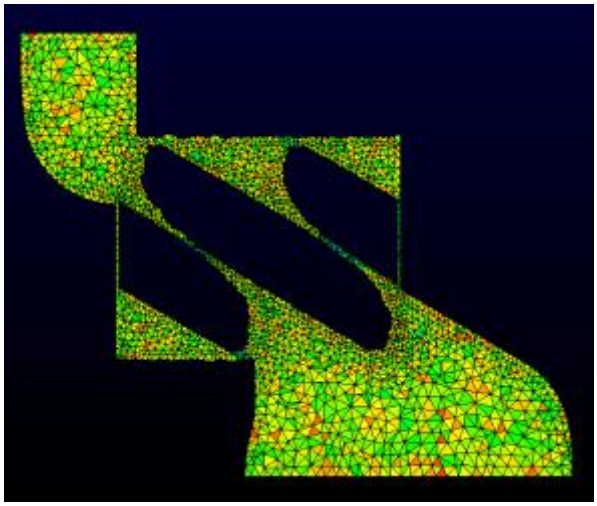

Figure 6: Interior axial plane mesh

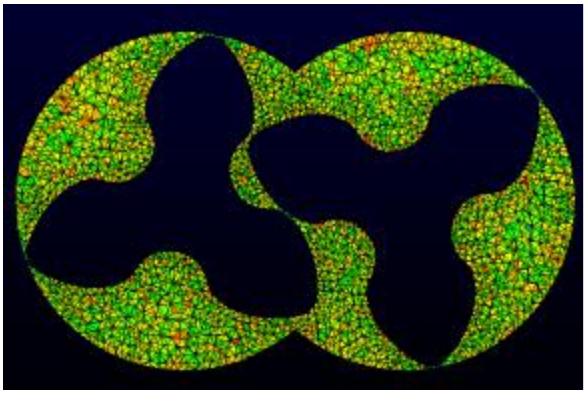

Figure 7: Interior radial plane mesh

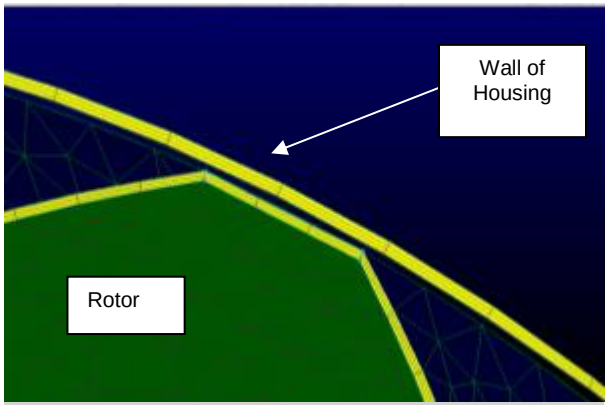

Figure 8: Refined mesh (highlighted in yellow) between rotor and S/C housing

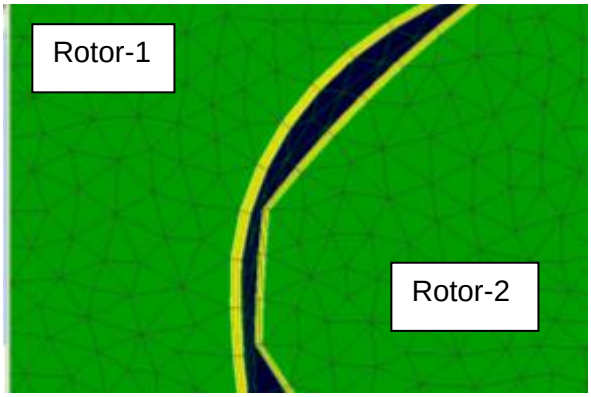

Figure 9: Refined mesh (highlighted in yellow) between each rotor

Even though the team was successful in performing CFD calculations using the first software tool, the calculations of torque did not correlate very well with the experimental data. Moreover, the CFD analysis was done with a 3-6 times larger than production gap between the rotors and housing. This increased gap width was used due to the difficulty in generating a refined mesh

with the available software. Hence, it was decided to acquire specialized software to be able to generate a refined mesh between the housing and rotor that is a few times less than the current production gap. The specialized software included a module that generated rotor profiles and a module that meshed the profiles. Figure 10 shows the template for inputting the rotors geometry data, and Figure 11 shows an image of the mesh generated by new software. Since the CFD analysis was performed with the rotors rotating, additional meshes were generated with the rotors at different positions. That is, each rotor was simulated to make one complete revolution and hence the rotor motion was divided into 468 steps and a mesh of the region around the rotors was generated at those 468 steps. A total of 936 mesh files were created (468 for each rotor).

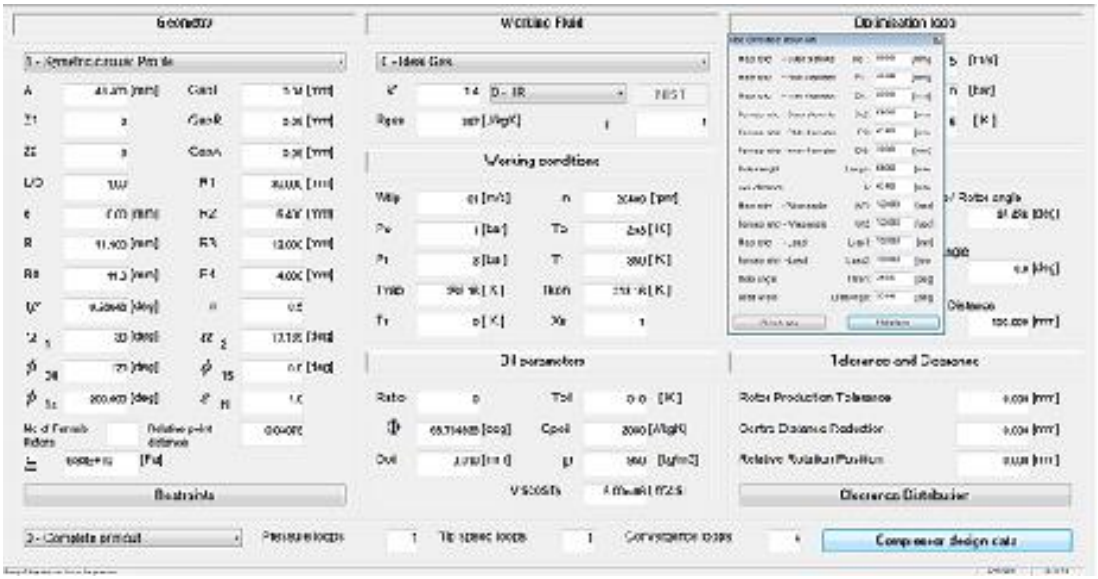

Figure 10: New software input template

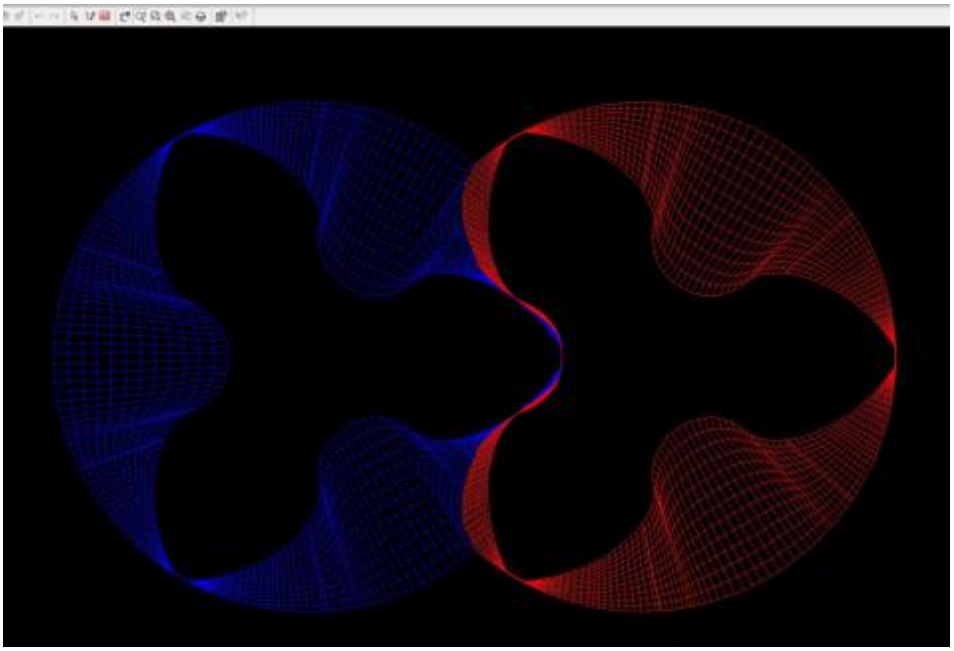

Figure 11: Mesh generated in new software

The 2nd CFD solver tool used for this analysis required generating separate meshes for the inlet and outlet regions and was combined with the mesh files from the new software. Figure 12 shows the completed geometry and mesh. The 968 mesh files generated in new software were then imported into 2nd CFD solver tool and were used during the CFD analysis. Using this procedure, mesh deformation was not used during the CFD analysis, but rather the new software meshes were used at the appropriate time-step.

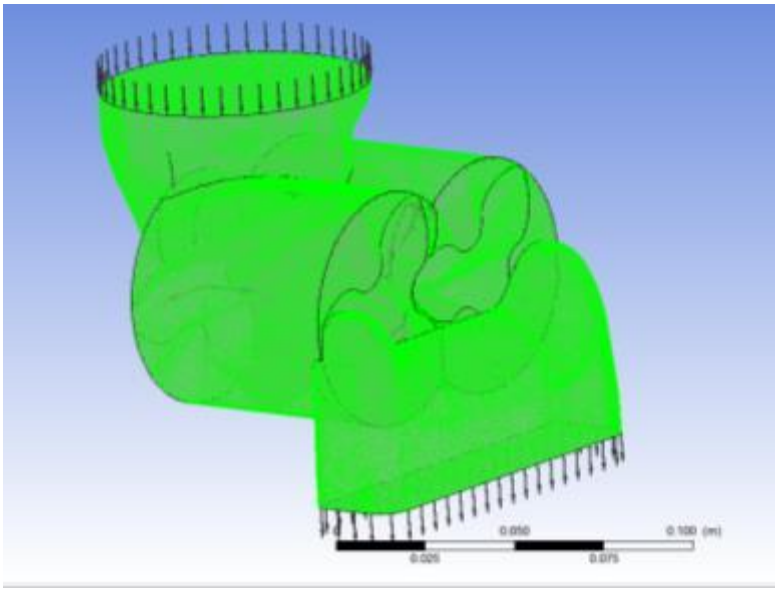

Figure 12: Complete mesh of unit

3.1.2 *Initial CFD Results and Comparison to Experimental Data:*

In order to determine the accuracy of the results from the methodology just described, two cases were considered. In both of these cases the supercharger-expander given in 1 was simulated with the following conditions:

Table 2: Operating conditions used in the numerical simulations

Parameter	Case 1	Case 2
Inlet Pressure	220 kPa (absolute)	140 kPa (absolute)
Outlet Pressure	100 kPa (absolute)	1000 kPa (absolute)
Rotational Speed	10,000 RPM	2,000 RPM

Transient CFD calculations were performed in both cases to simulate a complete revolution of the rotors. Constant density air at 25°C was considered to enter the unit at the inlet. The numerical simulations included calculating the velocity field, pressure distribution, turbulence kinetic energy and dissipation, throughout the entire three-dimensional model.

Figures 13 and 14 show the results for Case 1, and Figures 15 and 16 show the results for Case 2. Figures 13 and 15 depict the calculated torque on both rotors as a function of time in terms of the number of simulation time-steps for Case 1 and Case 2, respectively. Similarly, Figures 14 and 16 show the inlet and outlet mass flow rates as a function of time for Case 1 and Case 2, respectively.

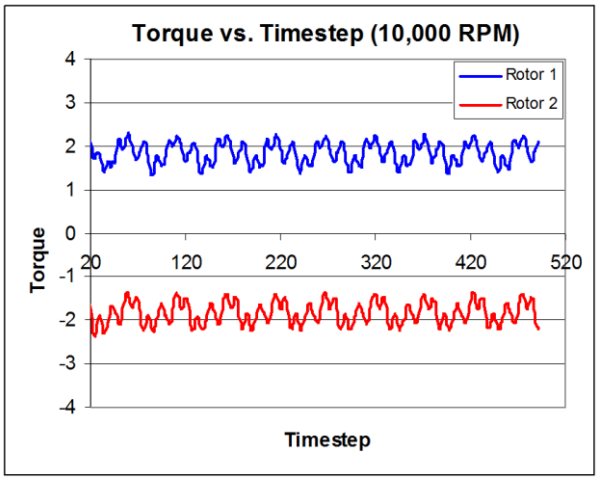

Figure 13: CFD results showing calculated torque in CFX on both rotors for the 10,000 RPM case

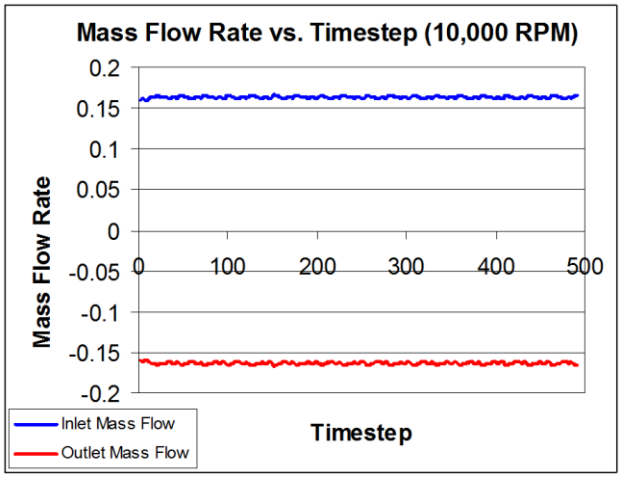

Figure 14: Inlet and outlet mass flow rates calculated in CFX for the 10,000 RPM case

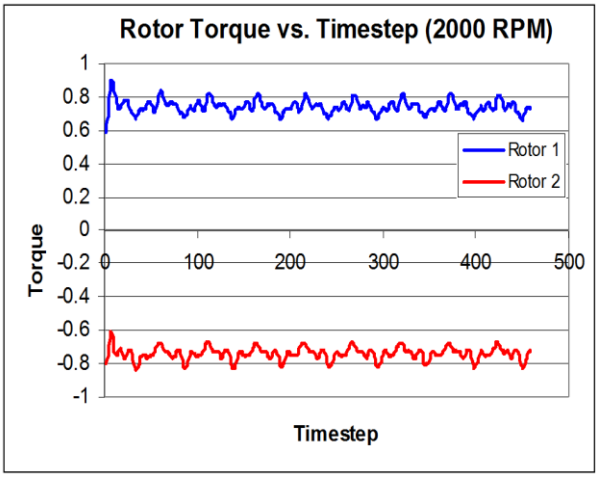

Figure 15: CFD results showing calculated torque in CFX on both rotors for the 2000 RPM case

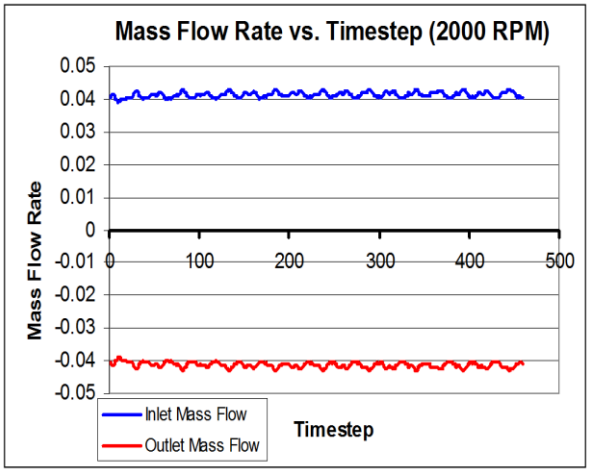

Figure 16: Inlet and outlet mass flow rates calculated in CFX for the 2000 RPM case

In order to verify the CFD results performed in 2nd CFD solver tool, the average calculated values of torque and mass flow rates were compared with the experimental data. A summary of the comparison are listed in Table 3 and Table 4.

Table 3: Comparison between numerical results and experimental data for Case 1

Parameter	Experimental	Numerical
Inlet Pressure (kPa abs.)	211	220
Outlet Pressure (kPa abs.)	101.9	101.3
Inlet Temperature (C)	147.8	25
RPM	10067	10000
Average Rotor Torque (N.m)	4.13	3.74
Average Mass Flow Rate (kg/s)	0.089	0.160

Table 4: Comparison between numerical results and experimental data for Case 2

Parameter	Experimental	Numerical
Inlet Pressure (kPa abs.)	142	140
Outlet Pressure (kPa abs.)	101.1	101.3
Inlet Temperature (C)	95.8	25
RPM	2041	2000
Average Rotor Torque (N.m)	1.615	1.47
Average Mass Flow Rate (kg/s)	0.021	0.041

In both cases, the calculated average torque was about 9% lower than the measured experimental values. In order to compare the mass flow rates we have to adjust the calculated values to the air inlet temperature used during the experiments, since in the CFD calculations air with constant density at 25 C was used. The calculated mass flow rate was adjusted as follows:

Mass Flow Rate = Air density x Volume Flow Rate

$\text{Air Density} = \frac{p}{RT}$, where *p* is absolute pressure, *T* is absolute temperature, and *R* is the gas constant for air.

$$\left(\text{Mass Flow Rate}\right)_{@T_{in}} = (\text{Mass Flow Rate})_{@25C} \times \frac{298}{T_{in}}$$

So, for Case 1 the adjusted mass flow rate is: $0.16 \times \left(\frac{298}{147.8+273}\right) = 0.113 \text{ kg/s}$ which is 27% higher than the experimental value. For Case 2, the adjusted mass flow rate is: $0.041 \times \left(\frac{298}{95.8+273}\right) = 0.033 \text{ kg/s}$ which is 51% higher than the experimental value. This difference could be due to the gap width in the unit used in the experiments was higher than the gap width used in the CFD model. Moreover, thermal expansion of the housing on the experimental unit could have occurred during the experiments which would result in a wider gap width.

The next step in the modeling process was to better understand the air flow through, and the performance of, various configurations of expanders and compressors.

3.1.3 *Expander CFD Results*

The CFD analysis demonstrated that the modeling process being used was accurately predicting improvements trends to expander geometric changes. There were a total of ten (10) expander geometries and configurations analyzed. All were compared to the baseline V250 expander configuration.

1. Configuration #1 - a V250 expander geometry with divider #2
2. Configuration #2 - a V250 expander geometry with divider #4
3. Configuration #3 - a V250 expander geometry with an extended inlet
4. Configuration #4 - a V250 expander geometry with bearing clearances added
5. Configuration #5 - a V250 expander with half the tip clearances and no end clearances
6. Configuration #6 - a V210 expander with the 1st outlet geometry as shown in Figure 17

7. Configuration #7 - a V210 expander with the 2nd outlet geometry as shown in Figure 17
8. Configuration #8 - a V210 expander with the 3rd outlet geometry as shown in Figure 17
9. Configuration #9 - a V210 expander with the 2nd geometry with bearing clearances added
10. Configuration #10 - a V210 expander with the 1st geometry and half the tip clearances and no end clearances.

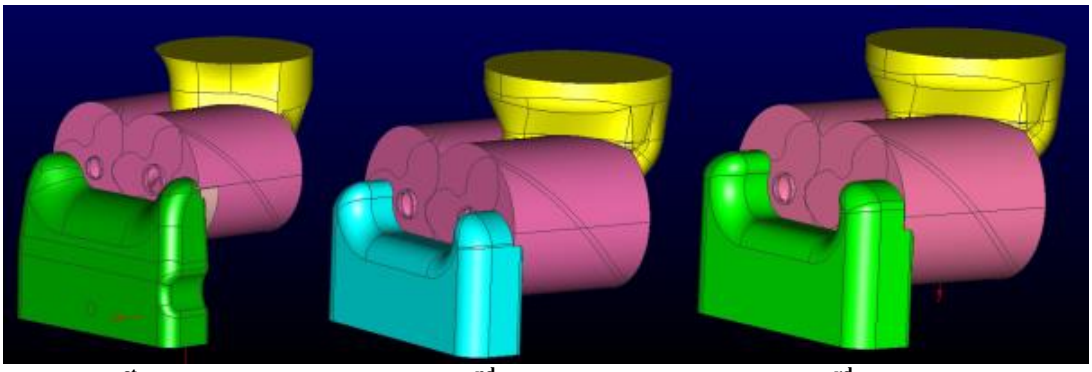

1st Geometry 2nd Geometry 3rd Geometry

Figure 17: Expander Outlet Geometries

The V250 and V210 expander units were three-lobe rotors. By the end of the program modeling the three-lobe rotors become a straight forward process for the CFD team. Mesh generation of the geometries was performed using the proprietary software and transient, three-dimensional CFD analysis was accomplished using the 2nd CFD solver tool.

Table 5: Expander CFD Results

	RPM	Boost	Mass Flow (g/s)			Torque (N.m)			Power (W)			Tin (C)	Tout (C)
			CFD	Base	% diff	CFD	Base	% diff	CFD	Base	% diff		
1	2100	1.4	24.63	25.33	2.76	1.51	1.54	1.94	332	338	1.77	90	75-76
2	2100	1.4	25.33	25.33	0	1.51	1.54	1.94	334	338	1.18	90	75-76
3	2100	1.4	25.38	25.33	-0.19	1.54	1.54	0	338	338	0	90	75-76
4	2100	1.4	26.15	25.33	-3.23	1.53	1.54	0.64	337	338	0.29	90	75-76
5	2100	1.4	20.53	25.33	18.9	1.53	1.54	0.64	336	338	0.59	90	45-76
6	2100	1.4	25.04	25.33	1.14	1.31	1.54	14.93	289	338	14.49	90	73-82
7	2100	1.4	24.07	25.33	4.97	1.31	1.54	14.93	290	338	14.20	90	73-82
8	2100	1.4	24.43	25.33	3.55	1.32	1.54	14.28	290	338	14.20	90	73-82
9	2100	1.4	24.53	25.33	3.15	1.31	1.54	14.93	290	338	14.20	90	73-82
10	2100	1.4	18.06	25.33	28.7	1.31	1.54	14.93	289	338	14.49	90	73-82

	RPM	Boost	Mass Flow (g/s)			Torque (N.m)			Power (W)			Tin (C)	Tout (C)
			CFD	Base	% diff	CFD	Base	% diff	CFD	Base	% diff		
1	10,000	2.2	93.07	97.19	4.24	4.17	4.39	5.01	4380	4590	4.58	150	88-93
2	10,000	2.2	95.53	97.19	1.71	4.29	4.39	2.28	4480	4590	2.40	150	88-93
3	10,000	2.2	97.95	97.19	-0.78	4.38	4.39	0.23	4580	4590	0.22	150	88-93
4	10,000	2.2	99.11	97.19	-1.98	4.35	4.39	0.91	4560	4590	0.65	150	85-93
5	10,000	2.2	89.70	97.19	7.71	4.38	4.39	0.23	4590	4590	0.00	150	85-93
6	10,000	2.2	87.72	97.19	9.74	3.81	4.39	13.21	3989	4590	13.09	150	84-95
7	10,000	2.2	86.67	97.19	10.82	3.81	4.39	13.21	3989	4590	13.09	150	84-95
8	10,000	2.2	87.67	97.19	9.80	3.83	4.39	12.76	4014	4590	12.55	150	84-95
9	10,000	2.2	87.68	97.19	9.78	3.80	4.39	13.44	3984	4590	13.20	150	84-95
10	10,000	2.2	77.52	97.19	20.24	3.83	4.39	12.76	4007	4590	12.70	150	84-95

The conclusions from the CFD results demonstrated that all changes to date only affect the flow performance and therefore expander efficiency, and not the torque or power performance at the modeled speed. The expander configuration #1 and #2 demonstrated that the diverter can improve flow performance but it has to be designed correctly. Diverter 2 reduced mass flow but diverter 4 had no effect. Expander configuration #3 with its extended inlet had no effect on flow performance at all. For the expander configuration #4, adding the bearing clearance cased mass flow to increase as expected but it did not increase appreciably. For the expander configuration #5, reducing the rotor tip and end clearances did decrease the mass flow significantly. Expander configuration #6, #7 and #8, had their outlet geometry modified and the results showed that it had some effect on flow performance but it was not significant (significant was defined as >2g/s). Configuration #7, the 2nd outlet geometry, had the largest flow performance improvement. Expander configuration #9 and #10 were similar modification to that of configurations #4 and #5 and the results show similar improvements.

In conclusion, the expander modeling demonstrated that some geometry modification, such as diverter and outlet geometries, can improve flow performance. The item that affected the flow performance the most was the rotor tip and end clearances. Therefore close attention was paid to tightly controlling these clearances.

3.1.4 *Compressor CFD Results*

In addition to the expander modeling, CFD modeling was conducted on the Roots compressor geometry. The first analyzed was the V250 compressor. All conditions were compared to a baseline.

The three lobed compressors modeled using the same tools as that used with the expanders proved successful. Comparisons of the CFD results with benchmark data show that the CFD mass flow results are within 1 – 12% of the benchmark data, and the torque calculations are within 10 – 30% of the benchmark data. It was believed this difference was due to numerical error, round-off error, and to effects not captured by the CFD modeling such as mechanical resistive torque due to bearings and gears in the rotor-shaft assembly, and variable clearances due to uneven thermal expansion of the rotors and housing. Four compressor speeds and four pressure ratios were analyzed with the CFD tool. Below are the average values of the total torque, inlet mass flow rate, and power for the conditions modeled.

Table 6: V250 Compressor CFD Results & Comparison with Baseline Data

RPM	Boost	Mass Flow (g/s)			Torque (N.m)			Power (kW)			Tin (C)	Tout (C)
		CFD	Base	% diff	CFD	Base	% diff	CFD	Base	% diff		
4,090	1.2	10.09	9.05	11.5	0.80	1.13	-29.2	0.343	0.48	-28.5	20	43
6,083	1.5	13.15	12.67	3.79	1.98	2.24	-11.6	1.27	1.43	-11.1	20	66
10,105	1.2	40.40	40.09	0.77	0.84	1.21	-30.6	0.89	1.28	-30.4	21	42
10,105	1.4	36.05	35.98	0.19	1.62	1.99	-18.6	1.71	2.11	-19.0	21	58
10,105	1.6	32.27	32.20	0.22	2.38	2.72	-12.5	2.53	2.88	-12.2	21	72
20,110	1.2	89.85	90.40	-0.61	1.05	1.24	-15.3	2.22	2.61	-14.9	23	44
20,110	1.4	86.43	87.26	-0.95	1.80	2.00	-10.0	3.77	4.22	-10.7	23	59

Below are a couple of example plots, Figures 18 & 19, at 4090 RPM and 1.2 boost, of the compressor torque curve as a function of angle of rotation for Rotor 1 and Rotor 2, and the mass flow rate at the compressor inlet.

Example Plots, at 4090 RPM and 1.2 boost

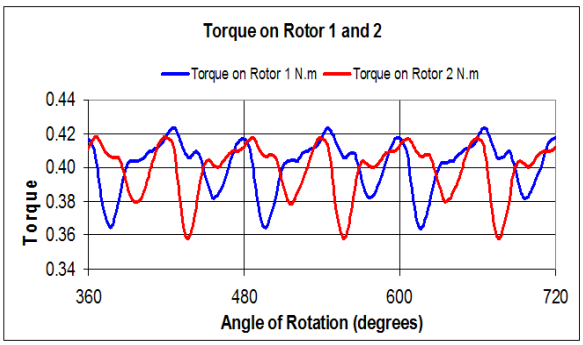

Figure 18: Torque Profile vs. Rotor Angle

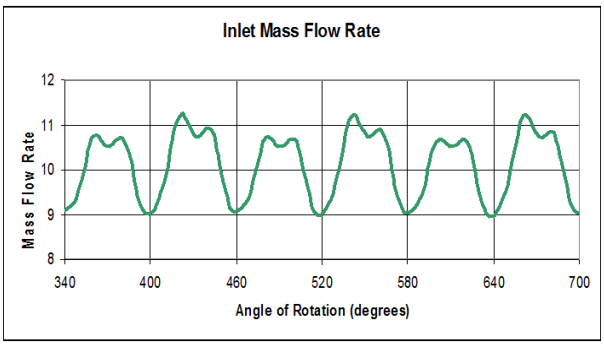

Figure 19: Mass Flow vs. Rotor Angle

The results show that the torque values are a strong function of the pressure ratio across the unit and are not significantly dependent on the rotational speed of the rotors. The torque increases with pressure ratio. However, the mass flow rate depends on both the pressure ratio and speed of rotation of the rotors. The low rate increases with RPM and is directly proportional to pressure ratio in expander configuration, but is inversely proportional to pressure ratio in compressor configuration.

The R410 compressor was analyzed to develop the capability of modeling four lobe compressors and to better understand the performance characteristics of this type of compressor. When the first set of models were run it was discovered that the proprietary meshing software would not work at the correct rotor clearances. In order to get the rotors to mesh without errors, the clearances had to be increased. The consequence was that the results had more leakage included in the flow numbers and had a greater error when compared to the test data. After discussing the issue with the proprietary software developers, the software was modified and a mesh for the 4-lobe rotors generated successfully. Transient, three-dimensional CFD analysis of the R410, P260 & V260 compressors units was completed.

The 260 4-lobe compressor with reduced clearances had inconclusive results when modelled. The software was incapable of resolving a 4-lobe geometry with high helix angle. The mass flow rates were considerably less than experimentally possible at the given operating conditions.

The 260 3-lobe compressor CFD analysis was run with various inlet geometries, Figure 20. The inlet timing was increased & decreased by +1 & -1 mm and +2 & -2 mm from the baseline geometry. The results show that these variations did not result in any significant changes in the mass flow rate and efficiency compared to the baseline values.

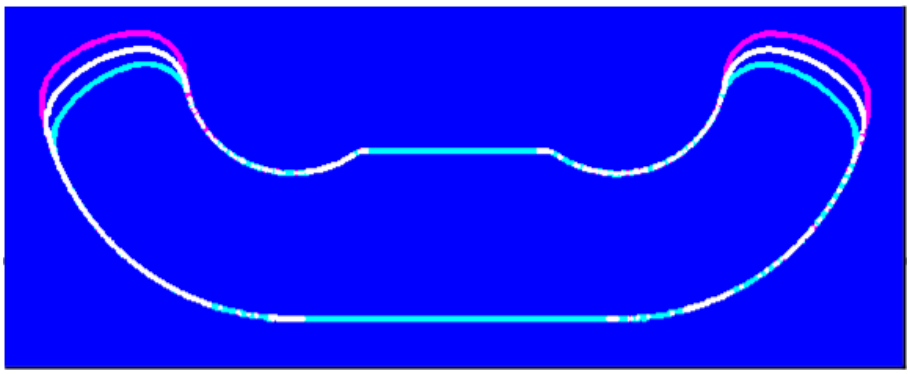

Figure 20: 3-Lobe Inlet to Rotors Area Variations

In summary, the results show that for the expander units, larger clearances between the rotors and the housing result in an increase in the mass flow rate. The effect of decreasing the clearances on average torque values was insignificant. Moreover, the shape of the torque curves depends on the rotational speed of the rotors and the pressure ratio across the rotors. At high speeds the rotors are able to move the air through the outlet faster than air can flow into the inlet, thus causing a decrease on the high pressure side on the rotors resulting in a decrease of the torque. This suggests that the position of the inlet and outlet relative to the rotors can have an effect on the power output and efficiency of the unit.

3.2 Plastic Component Development

The goal in the development of the expander for the fuel cell application was to develop a low cost, small displacement, (4.6 to 92 g/s flow rate), high pressure ratio (1.2 to 2.5 bar) and efficient (200 W_e to 14 kW_e) design. The primary technical challenge was the small displacement due to the ratio between the rotor leakage and the displaced volume. As Roots devices are downsized, the rotor tip to root & rotor tip to housing leakages increase to a point that they dominate the overall mass flow and results in the efficiency to dropping off significantly. The goal was be to minimize leakages and determine the right displacement vs. speed to optimize the device performance for the application. Additionally, since the specification required improved performance over a broad operating range; optimization was focused on the middle to high operating range of the device.

The program investigated several concepts to attempt to meet the performance requirements and reduce product cost. The concepts are outlined below:

1. Straight Rotor
2. Helical Rotor
3. Plastic Housing, End Plate and Gears

3.2.1 *Plastic Expander Rotor Analysis*

In the development of the plastic rotors Finite Element Analysis (FEA) of various rotor configurations was completed. The results indicated a 60% reduction in stress with the baseline 4 lobe design over the baseline 3 lobe design as shown in Figure 21. Even with a 60% reduction in stress, the four lobe design is more than twice the expected limits for the plastic chosen. Experimental testing shows part failure in the same location as predicted by the analysis. To reduce the stresses to the acceptable range an improved rotor design was created and analyzed.

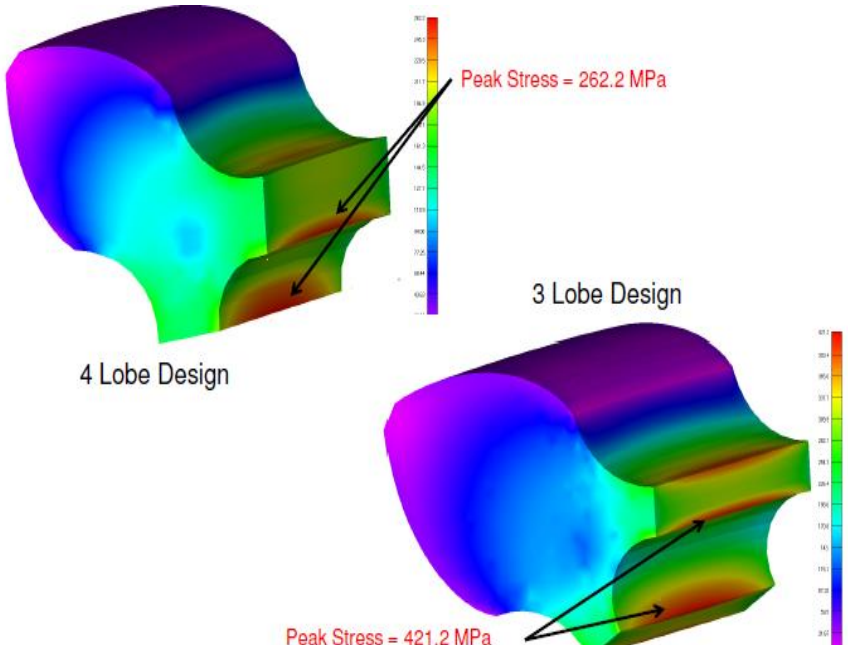

Figure 21: FEA of 3 and 4 Lobe Plastic Rotors

To resolve the stress issue an optimized 4 lobe rotor design with the addition of an extruded aluminum sub-frame was developed. The intent of the aluminum sub-frame is to provide support and stiffness in the high stress root region as well as provide a mechanical lock to improve the adhesion in the lobe. Table 7 shows the stresses and achieved speeds (rpm) at 150°C for four designs that were evaluated. The failure mechanism for all designs occurred when the composite delaminates from the aluminum extrusion at the mechanical locking feature. Design iteration 4 achieved 20,000 rpm although the stresses exceeded the capability of the glass reinforced composite. The application under consideration does not exceed a temperature of 70°C and as this analysis was done at a maximum temperature of 150°C, design four was considered acceptable.

Table 7: Summary of FEA results at 150°C

Design Iteration	Comments	Speed Achieved (rpm)	Max Principal Stress of Composite (MPa)
1	 Unable to run due to lack of mechanical features – composite separated from aluminum extrusion	N/A	179
2	 addition of mechanical locking feature along length of lobe	8000	258
3	 Dovetail interlock along diameter and at the tip of the root	12500	644
4	 Reduced height of aluminum extrusion into the lobe; simplified geometry of dovetail	20,000	614

Based on the FEA results a tool design was initiated that would allow for molding of a polymer rotor with or without the aluminum support. The runner system for the rotor injector mold was optimized through mold flow simulations. Initial design was a pin gate located at the tip of each of the four lobes, refer to Figure 22. Fibers were highly oriented at the gate location on the lobe tip and became increasingly more random towards the root, Figure 23. In an effort to increase fiber orientation at the root, and thereby increase the root strength, a second runner system was designed and evaluated, Figure 24. The final design had a runner system with 8 pin gates that were located in the root at two points. The resulting fiber orientation increased the alignment in the root region with random fiber orientation at the tip Figure 25.

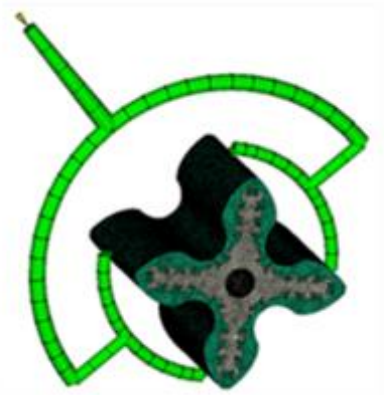

Figure 22: 4 pin runner system

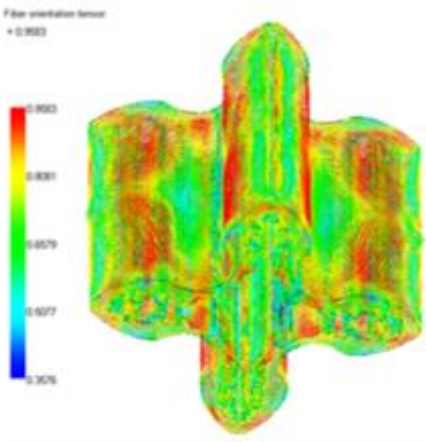

Figure 23: Fiber orientation with red being highly oriented and blue being random

Figure 24: 8 pin runner system

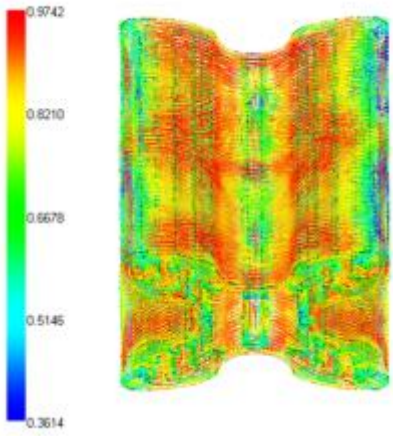

Figure 25: Fiber orientation with red being highly oriented and blue being random

3.2.2 *Straight Rotor Hardware Development*

Plastic rotors with the above mentioned aluminum support structure was fabricated. Figure 26 shows the process to assemble the tool. There were 6 inserts to form the rotor lobes and allow

for the runner system to be gated at the root. The aluminum support structure was press fit onto the shaft and loaded into the tool, the shaft protrudes into the base of the tool. As a contingency plan billet aluminum rotors were also procured.

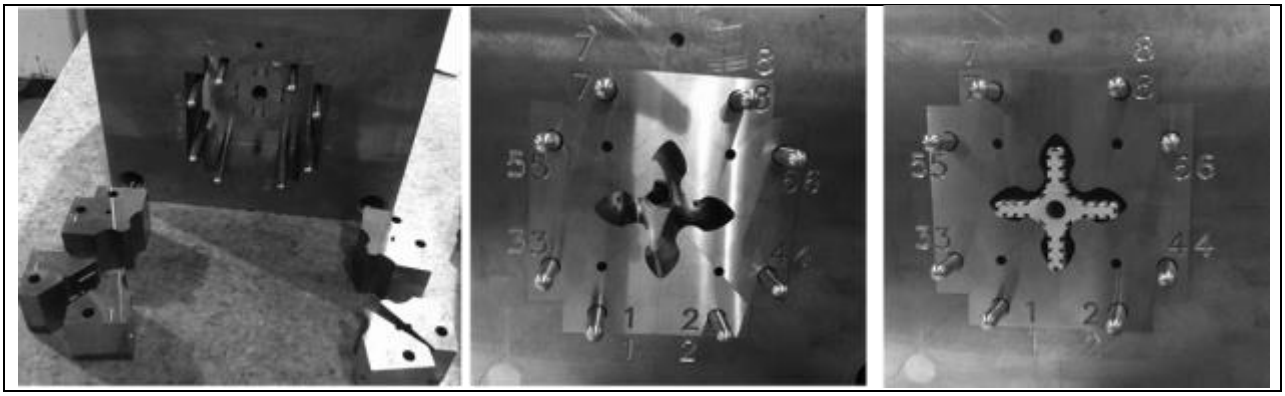

Figure 26: Tool design has 6 segments to form the rotor lobes while allowing for the runner system. Once the 6 segments are assembled the shaft and aluminum support structure are loaded (locating pins are present for alignment).

Upon completion of procurement, Figures 27 & 28 spin testing of the rotors was completed at speeds of 15,000, 17,500 and 20,000 at a constant temperature. Testing was conducted at three temperature set points – 70C, 90C and 100C with dwell times of 5 minutes. The over-molded rotor was able to achieve the maximum rpm at maximum temperature (20,000 rpm at 110C) with no evidence of delamination.

Figure 27: As molded rotors. Component completely filled with no evidence of delamination or porosity

Figure 28: Rotor posttest (conditions 20,000 rpm at 110C). No failure and no indication of delamination. Scuff marks from contact with housing delamination from the aluminum support structure.

3.2.3 *Helical Rotor Hardware Development*

Due to the successful testing of the straight plastic rotors, the development of the helical shape rotors proceeded. The straight aluminum support structure, as seen in Figure 29, was revised

to accommodate a helical rotor. Interlocking features were optimized to increase polymer adhesion. FEA was used to validate the helical design and material selection, as seen Figure 30.

Figure 29: As Molded Straight Rotors

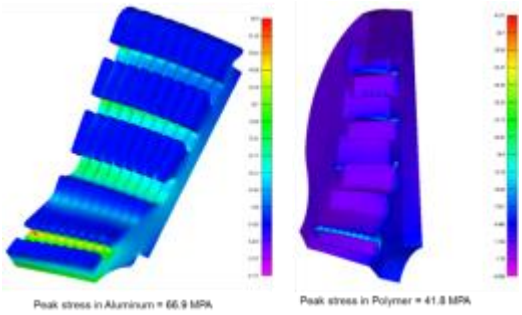

Figure 30: FEA of helical overmold rotor; validation of interlocking design

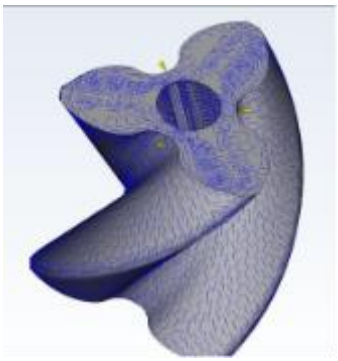

Figure 31: Mold Flow Results showing fiber orientation

Mold flow analysis was completed and gate configuration designed to optimize fiber orientation for hoop strength, as shown in Figure 31. Tooling was designed and fabrication of components was completed. Figure 32 shows the completed prototype of the aluminum support structure for the rotors. These components were manufactured via an additive manufacturing process and were chosen due to the quantity of pieces ordered, timing and part complexity.

Figure 32: Additive Manufactured Aluminum Support Structure

Figure 33: Rotors overmolded onto aluminum support structure

The aluminum support structures were press fit onto the steel rotor shafts and loaded into the injection molding machine for overmolding with polymer. Both right hand and left hand rotors were molded, as seen in Figure 33. The rotors were finished with a coating which reduces rotor-to-rotor and rotor-to-housing clearances. The rotors were tested at a maximum speed of 12000 rpm and pressure ratio of 1.5 bar without failure.

3.2.4 *Plastic Housing, End Plate and Gears*

An expander containing plastic rotors, housing, end plate, and gears was developed and experimentally evaluated, Figure 34. During testing, the unit was run up to a maximum of 18000 rpm and pressurized to maximum of 2.0 pressure ratio at 130°C without failure. The plastic expander clearances were larger than that of a comparable aluminum unit due to the tolerance capability of the plastic injection molding process. These large clearances are a result of the tolerance capability of the plastic injection molding process. The clearances can be significantly improved with further adjustments to the housing and rotor molds.

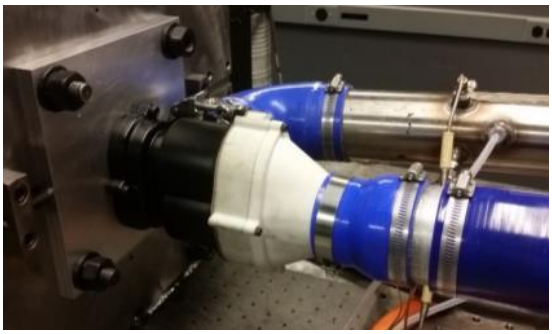

Figure 34: Plastic V210 Expander on Test Stand

3.3 Compressor Development

The goal in the development of the expander for the fuel cell application was to develop a small displacement, (4.6 to 92 g/s flow rate), high pressure ratio (1.2 to 2.5 bar) and efficient (200 W_e to 14 kW_e) design. The primary technical challenge was the small displacement due to the ratio between the rotor leakage and the displaced volume. As Roots devices are downsized, the rotor tip to root & rotor tip to housing leakages increase to a point that they dominate the overall mass flow and results in the efficiency to dropping off significantly. The goal was be to minimize leakages and determine the right displacement vs. speed to optimize the device performance for the application. Additionally, since the specification required improved performance over a broad operating range; optimization was focused on the middle to high operating range of the device.

The three target specifications for the compressor operated at 40°C, 25% relative humidity inlet conditions are as follows.

1. High flow rate = 92 g/s flow rate, pressure ratio = 2.5 bar and power = 14 kWe
2. Middle flow rate = 23 g/s flow rate, pressure ratio = 1.5 bar and power = 2 kWe
3. High flow rate = 4.6 g/s flow rate, pressure ratio = 1.2 bar and power = 200 We

The program investigated several concepts to attempt to improve the performance of Roots compressors. The concepts are outlined below:

1. High Pressure Recirculation - Directing high pressure, high velocity air from the outlet of the compressor to the back of the rotor housing, with a particular timing. The concepts goal was to reduce the back rush of air at the outlet thus reducing temperature and increasing the ultimate pressure ratio capability of the compressor.

2. High Helix Rotor - Assessment of short rotor designs with increased helix angle to determine if higher pressure ratio can be achieved.

3. Low Thermal Growth Rotor - Investigation into the use of low thermal grow material so that closer tolerances can be held within the air cavity to reduce leakage, enabling higher pressure ratios and efficiencies.

3.3.1 *High Pressure Recirculation*

As a Roots compressor spins, it moves air trapped at ambient pressure, from the intake of the compressor to the positive pressure outlet. Once the air is released by the lobes, there is a back rush of pressurized air that compresses the air that was just released before it is pushed out by the next rotor lobe. This back rush of air is a contributor to the increased outlet air temperature of the compressor. A Roots compressor's maximum pressure ratio capability is limited by outlet air temperature and its impact on the materials exposed to these temperatures. Therefore, it was hypothesized that by directing high pressure, high velocity air from the outlet of the compressor to the back of the rotor housing, with a particular timing, the pressurized air's momentum and increased pressure would help to reduce the back rush of air at the outlet thus reducing temperature and increasing the ultimate pressure ratio capability of the compressor.

This theory was tested using an R340 compressor with a modified outlet to direct recirculated pressurized air to the rotor housing, and a modified housing to time and direct the pressurized air to the rotors, see Figure 35. The R340 was initially tested with the recirculation tube obstructed by a sealing gasket material. The test was then rerun with the recirculation port unobstructed and the results compared. Overall performance was reduced with the maps indicating an increase in leak rate, especially at higher speeds and pressure ratios. With leakage comes a loss and shift in the efficiency islands, an increase in power consumption and larger temperature differentials. There was an increase in the temperature differential of ten to twelve degrees Celsius at all points, thus limiting the compressor's maximum pressure ratio capability.

Figure 35: High Pressure Recirculation Setup

3.3.2 *High Helix Rotor*

Testing results have shown that the shortest rotor design provided the highest pressure ratio capability. Although inlet and outlet geometries vary by application, the consistent contributor to the increased capability, of the shortest rotor, is the increased helix angle. This can be seen when comparing the R340 map with the R410 map, seen in Figure 36. For experimental verification, the P400 was selected for testing, at increased pressure ratio, as it has the greatest helix angle of any Eaton prototype compressor to date, shown in Figure 37.

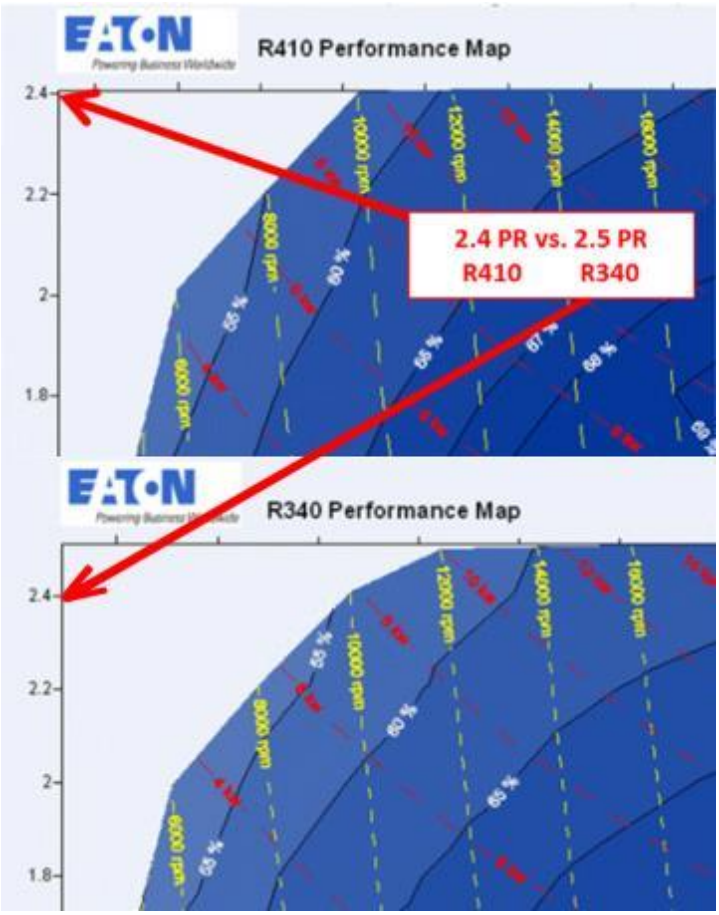

Figure 36: R410 vs. R340 PR Comparison

Figure 37: P400 Test Unit

Results of the P400 testing demonstrated that the increased helix angle pushed the P400 efficiency map to a pressure ratio over 2.6 without exceeding the maximum temperature of the unit.

3.3.3 *Low Thermal Growth Rotor Experiment*

The purpose of this experiment was to assess the use of low thermal growth material to maintain tight air cavity clearances. The intention was to reduce leakages, enabling higher pressure ratios and efficiencies. Figures 38 and 39 are the low thermal growth compressor rotors that were developed in both 3 and 4 lobe architectures for a 260cc/rev displacement compressor. These were made from a ferrous material and coated with an abradable material that should provide better compressor sealing. The rotor design utilized a low inertia architecture to minimize impact on acceleration speeds relative to the solid billet design.

Figure 38: 4-Lobe Compressor Rotors

Figure 39: 3-Lobe Compressor Rotors

The preliminary fabrication process introduced tolerances and distortions that were greater than the outlined specification. Due to timing, further development of this technology was halted on the program but Eaton development has continued on the concept.

3.3.4 *Final Compressor Design*

The final compressor design was a V250 compressor, see Figure 40. This is a 3-lobe compressor with a 247 cc/rev displaced volume.

- Rotors: The rotor set was optimized for midrange performance, in a three lobe design, with an increased helix angle to achieve the higher pressure ratios required by the DOE. The rotors were made from the traditional Eaton prototyping process; they are machined from aluminum billet. Tolerances are tightly controlled to keep clearances low to maintain good compressor efficiency.
- Housing: The housing design featured an optimized outlet geometry as well as an integrated motor adaptor plate. The housing utilizes existing Eaton production seals, bearings, and gears to reduce cost.
- Gears: The timing gears were an existing Eaton steel design with water cooling shared with the electric drive motor to increase durability at high pressure ratios.

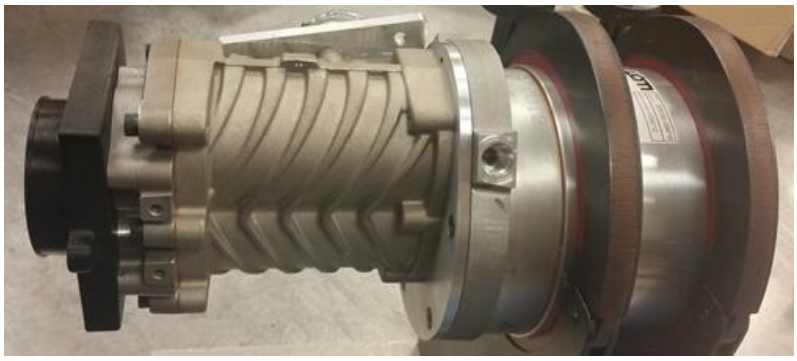

Figure 40: V250 Compressor

A full compressor map was created on the V250 compressor was qualified. Figure 41 shows the results.

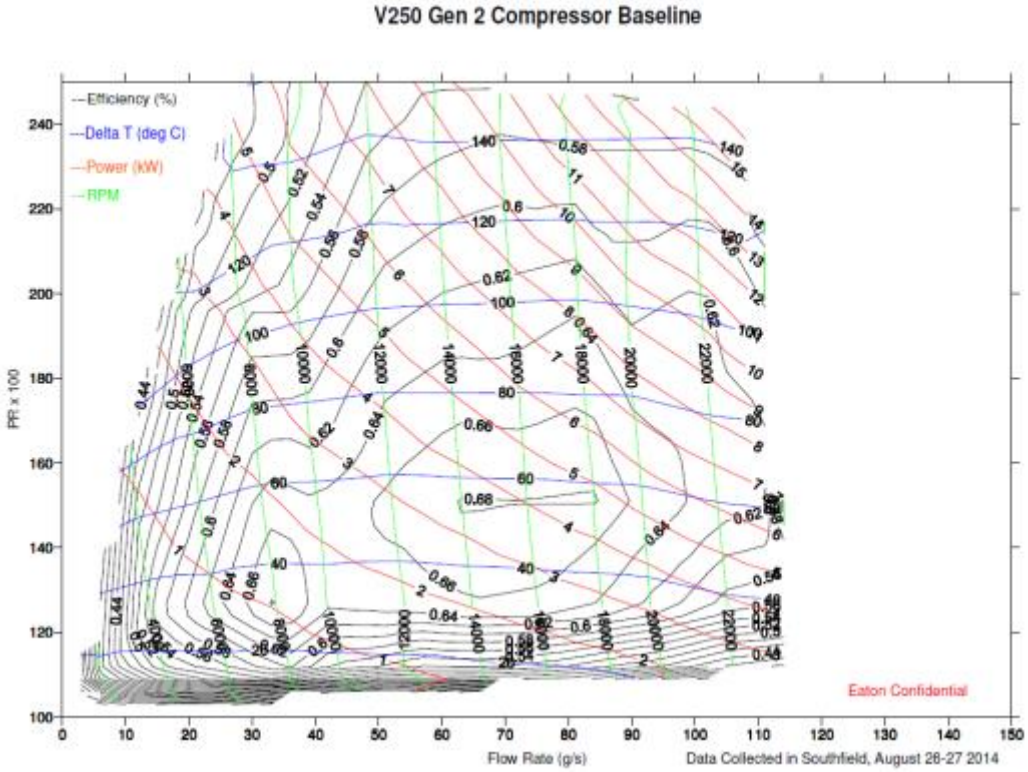

Figure 41: V250 Uncorrected Compressor Efficiency Map

3.4 Expander Development

The goal in the development of the expander for the fuel cell application is to develop a low cost small, (4.6 to 88 g/s flow rate), high pressure ratio (1.0 to 2.2 bar) and efficient (0 W_e to ~6 kW_e) design. The primary challenge in this program is the small displacement. This is due to the ratio between the rotor leakage and the displaced volume. As with the compressor design, as Roots expanders are downsized leakages increase to a point that they dominate the efficiency performance of the expander and cause the efficiency to drop off significantly. The goal will be to minimize leakages and determine the right size vs. speed design that optimizes the compressor performance for the application. It is possible that the optimal expander design might not match the compressors optimal speed range. If power is to be optimized, then a gear ratio might be required. Also, since the specifications drive for improve performance over a broad operating range; optimization will focus on the middle to high operating range.

The three target specifications for the compressor operated at 70°C, 100% relative humidity inlet conditions are as follows.

1. High flow rate = 88 g/s flow rate, pressure ratio = 2.2 bar and power = ~6 kWe
2. Middle flow rate = 23 g/s flow rate, pressure ratio = 1.4 bar and power = ~1 kWe
3. High flow rate = 4.6 g/s flow rate, pressure ratio = less than compressor pressure and expander does not provide any negative power (0 We)

The program investigated several concepts that were thought to improve the performance of Roots expander. They are:

1. Expander Baseline Experiments - An initial series of tests were conducted using non-modified Eaton compressors units in reverse direction.

2. Inlet Port Experimentation - Several inlet port configurations were built and tested in an attempt to characterize which inlet port attributes effect performance and improve the expander efficiency and power generation. The inlet configurations were varied by inlet angle, inlet diameter, and geometry near the rotor face.

3. Smaller Displacement Expander - A V170 expander was designed & built to characterize the effect of reduced displacement on operating speed and efficiency. It was built from a standard V250. .

4. Final Expander Design - A V210 expander was chosen as the compressor with the best performance for the final application.

3.4.1 *Expander Baseline Experiments*

At the beginning of the program very limited research had been done on the development of Roots expanders at Eaton. The initial series of test were conducted using non-modified Eaton compressors spun in the reverse direction. The tests were run on a dynamometer where pressurized air was flowed through the expander. The first series of tests were run on three units a R200, a V250 Gen 1 and a V250 Gen 2. The V250 Gen 1 was set as the expander baseline.

3.4.1.1 R200 Results

The R200 compressor design is different from the 3 lobe rotor V250 Gen 1 and Gen 2 since the R200 uses a TVS 4 lobe rotor and its displacement is 50 cc/rev less or 200cc/rev. This unit was first tested as a compressor to confirm the unit's performance and then tested as an expander in two configurations. The first expander configuration provided pressurized air to the compressor's inlet and the second configuration provided pressurized air to the outlet of the compressor. The compressor inlet and outlet are outlined in Figure 42. The pressurized outlet configuration depicted in Figure 42, proved to have best performance for the R200.

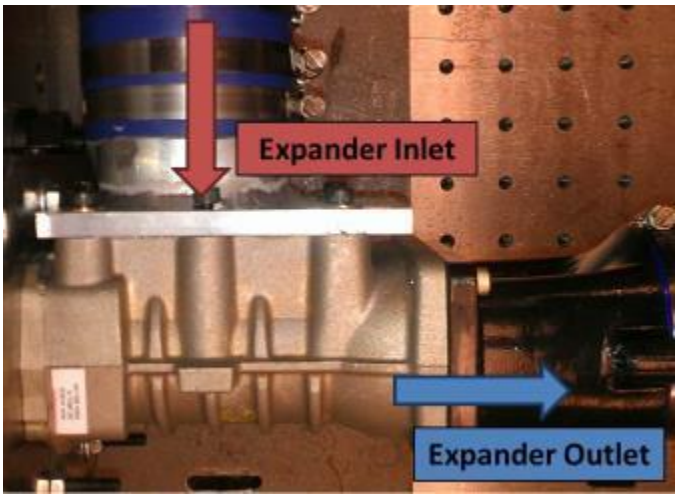

Figure 42: R200 with Pressurized Outlet

3.4.1.2 V250 Gen 2 Results

The V250 Gen 2 compressor shown in Figure 43 is different in design when compared to the V250 Gen 1 as changes to outlet geometry and rotor length were completed. Prior to expander testing, the V250 Gen 2 unit was first tested as a compressor to confirm the unit's performance. The first configuration as an expander provided pressurized air to the compressor's inlet (this is the axial flow end), Figure 43. The second configuration provided pressurized air to the outlet of the compressor (this is the perpendicular flow end), Figure 44. Historically, optimal performance of a compressor, as an expander, has been found by pressurizing the outlet of the compressor. This was true of the V250 Gen 2 as well.

When comparing the performance of the V250 Gen 2 to the V250 Gen 1 expander, the V250 Gen 2 did not produce as much power as the V250 Gen 1 at the 100% target but was slightly better at the 25% target.

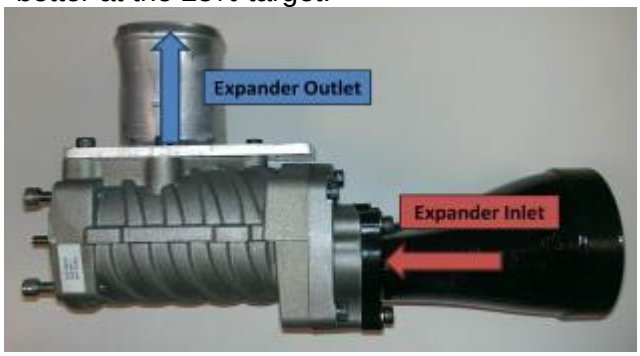

Figure 43: V250 Gen 2 with Pressurized Compressor Inlet

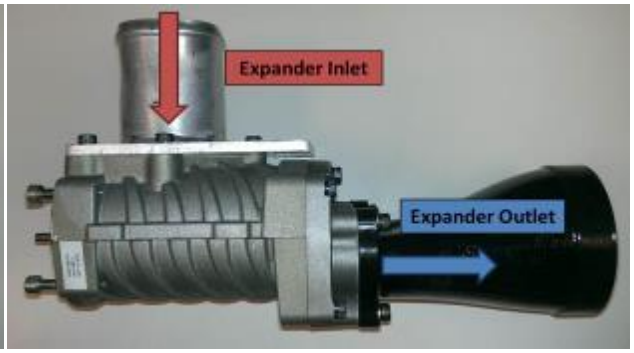

Figure 44: V250 Gen 2 with Pressurized Compressor Outlet

3.4.1.3 V250 Gen 1 Results

From the previous two sets of tests, it appeared that the V250 Gen 1 (Figure 45) had the best opportunity to produce the most power as an expander. As such, it was decided to use this unit as the baseline to investigate new designs or configurations.

3.4.2 *Inlet Port Experimentation*

Several inlet configurations were built and tested with the V250 Gen 1 unit in an attempt to characterize which attributes effect performance as well as further improve the efficiency and power generation. The inlet configurations were varied by inlet angle (Figure 46), inlet diameter (Figure 47), and geometry near the rotor face.

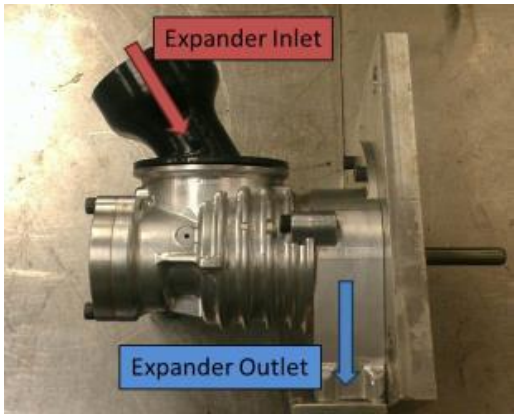

Figure 45: V250 Gen 1 Expander In & Outlet

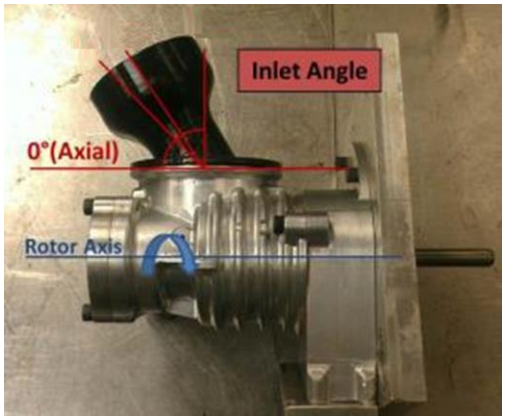

Figure 46: V250 Gen 1 Expander Inlet Angle

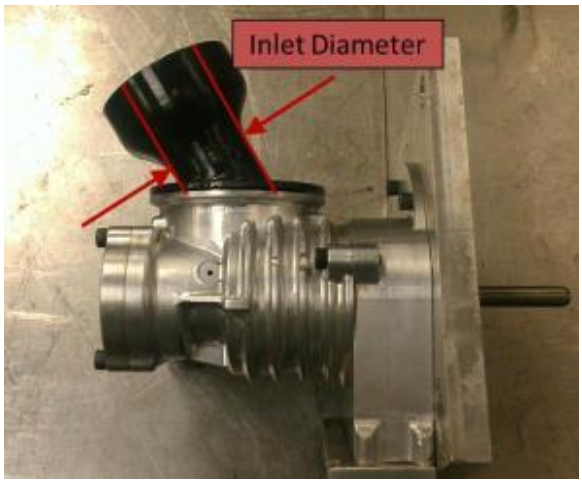

Figure 47: V250 Gen 1 Expander Inlet Diameter

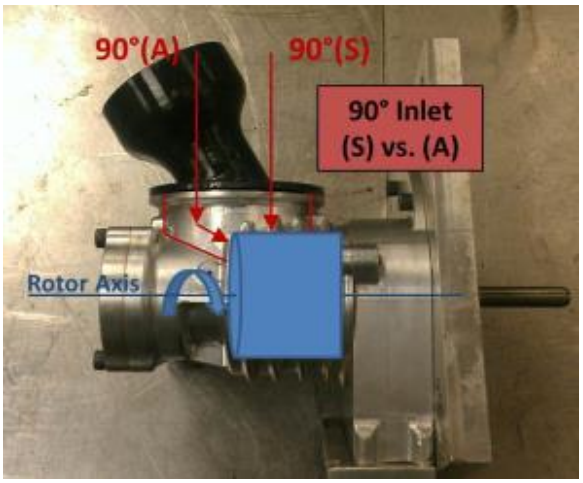

Figure 48: V250 Gen 1 Expander 90 deg (A) Inlet vs. 90 deg (S) Inlet

The results from the first round of intake testing were graphed and are given in in Figure 49. It is important to note that the inlets tested were created from ABS plastic with a maximum operating temperature of 115°C. This limited the upper pressure ratio capability of the test to 1.8 PR below the required DOE target of 2.2 PR. Mass flow rate was accurate for both 25% and 100% DOE targets. The reduced PR at 100% target influence the absolute values at that point however, the relative values illustrate the effect of the design changes. Nine tests were run on this unit when evaluating the inlet designs.

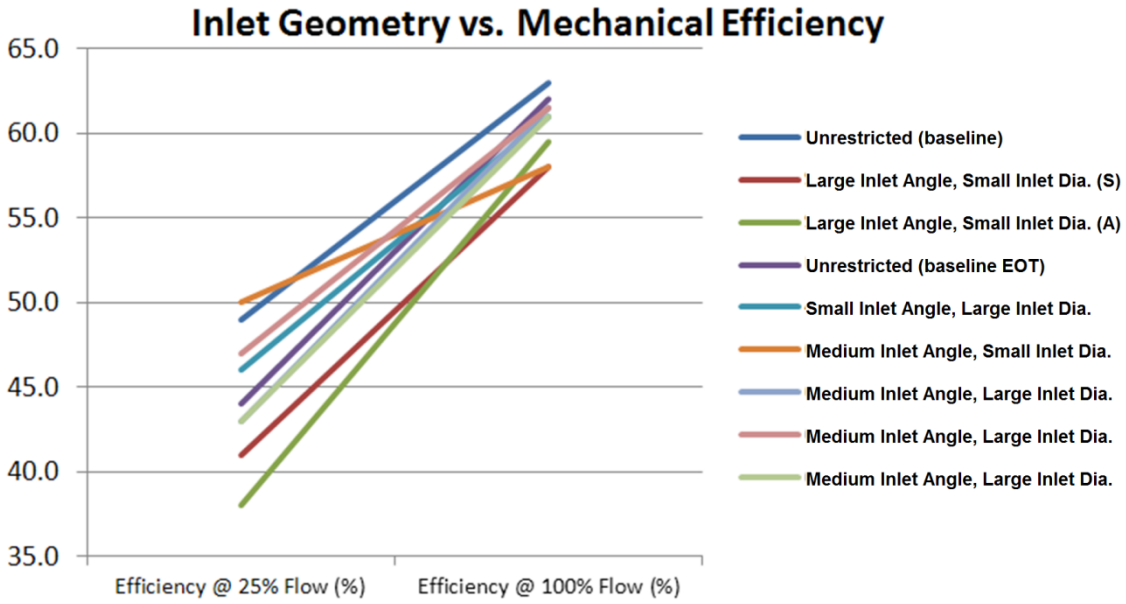

Figure 49: Inlet Test Results of V250 Gen 1 Expander

In summary, testing to this point suggested that an optimal inlet geometry for the V250 Gen 1 expander had the large inlet diameter, the small inclined angle and a means to directed air flow towards the outside of the rotor housing, see Figures 50 and 51.

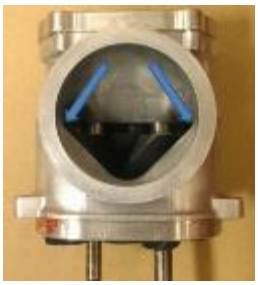

Figure 50: V250 Gen 1 Expander Inlet with Direct Air Flow Path

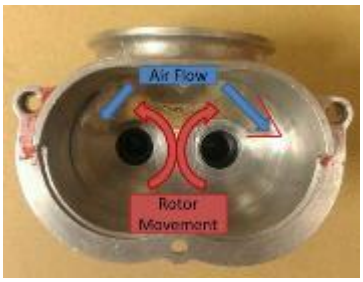

Figure 51: V250 Gen 1 Rotor Housing with Direct Air Flow Path

3.4.3 *Smaller Displacement Expander*

A V170 expander, Figure 52, was designed and built to assess a downsized expander. This is the smallest expander tested at Eaton to date. It was built using a standard V250 Gen 1, the one used in baseline testing, by adding shortened rotors and a fill plate to correct rotor timing and prevent additional air leakage. The V250 Gen 1 rotor has a length of 66 mm and a displacement of 247cc/rev. This rotor set was shortened to 44 mm in length equaling a 1/3 reduction in displacement to 165cc/rev.

The main objective of the V170 unit is to characterize the effect of reduced displacement on operating speed and efficiency. To meet the 100% flow target, the V170 test has a 41.5% increase in operating speed compared to the V250. Additionally, there is a reduction in isentropic efficiency of 5.5% at this point. This translates to a reduction in power output from 4.35 kW with the V250 baseline to 4.04kW for the V170 at the 100% flow target.

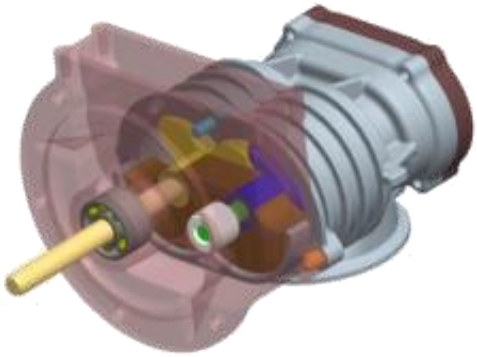

Figure 52: V170 CAD Model

3.4.4 *Final Expander Design*

A V210 expander was chosen as the displacement with the best performance for the application (refer to Figure 53 for a picture of the final assembly). The design features were as follows:

- Rotors: The rotor set was optimized for performance with a displacement of 210 cc/rev.

Figure 53: V210 Expander Assembly

- Housing: The housing was fabricated from Eaton's standard aluminum material and incorporated communized shaft, bearing, and seal sizes as well as improved inlet geometry.

- Outlet: The expander outlet was originally designed as a glass reinforced plastic part that locates the shaft ends with two incorporated sealed roller bearings with plastic dust covers. Three different plastic materials were evaluated; see Figure 54, to determine the lowest cost option that also met the expander requirements. The bottom right outlet aluminum and was the material used for the Ballard testing.

Figure 54: Expander Outlet Plates in Multiple Materials

- Timing Gears: The timing gears used an existing Eaton plastic/steel hybrid design. Figure 55 shows one of the two plastic timing gear materials that will be assessed.

Figure 55: Plastic Expander Timing Gears

- Step-up Gears:
- **Figure** 56: Steel Motor to Expander Step-Up Gears
- 56 shows the step-up gears that are used between the motor and expander. These gears were used to optimize the speed points between the compressor and expander. This set of gears drove the expander 2.2 times faster than the compressor.

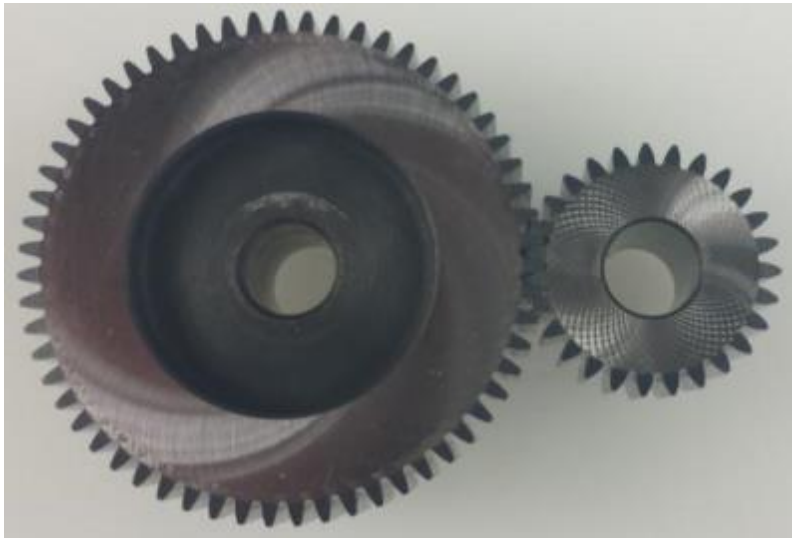

Figure 56: Steel Motor to Expander Step-Up Gears

3.5 Motor and Controller Testing

Eaton has worked with several motor OEM's over the years to apply their technologies to fuel cell applications. The intention from the start was to use motor and controller technologies previously developed and apply them here (Eaton had previously developed a 7 turn & 12 turn motor). A baseline motor and controller performance map was created using the 7 turn brushless DC motor and controller, Figure 57. The motor and controller map, was provided to Argonne National Labs for integration into the Fuel Cell System model.

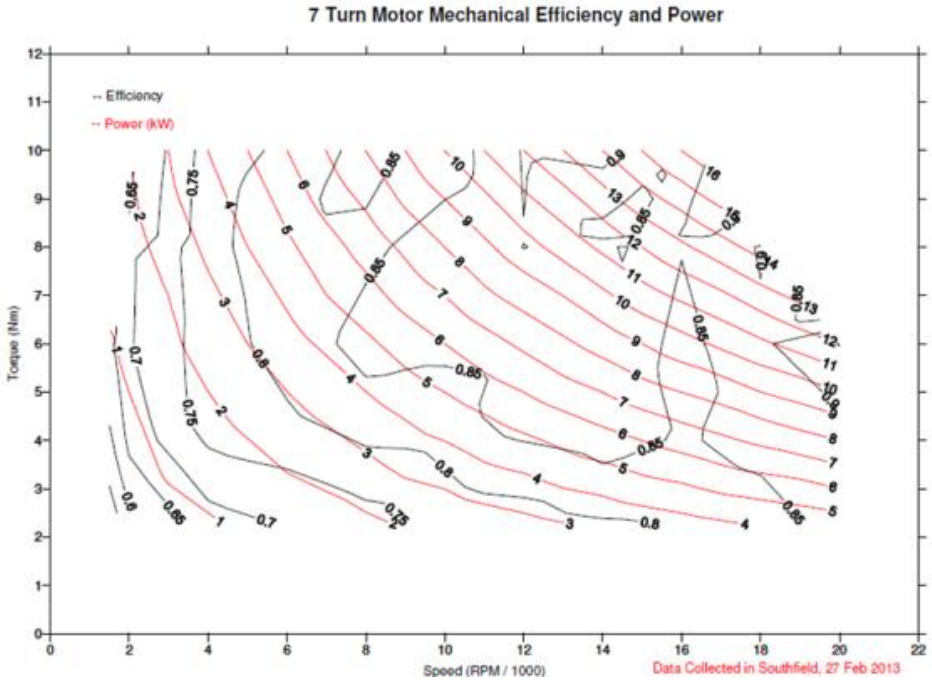

Figure 57: Motor and Controller Map

3.5.1 *Motor Design*

The final motor configuration used existing motor rotor & stator that was adapted for this application. In the development process it was determined that the 12 turn motor, which produced 16 kilowatts, was required for best efficiency and performance for the operating range of the air system. The motor supplier provided the controller, rotor, stator and stator housing. Eaton designed and fabricated the mounting for the expander and compressor to both sides of the motor. Figure 58 shows the electric motor layout with the end plates which incorporate the motor bearings, water cooling passages and the mating surfaces for mounting the expander and compressor.

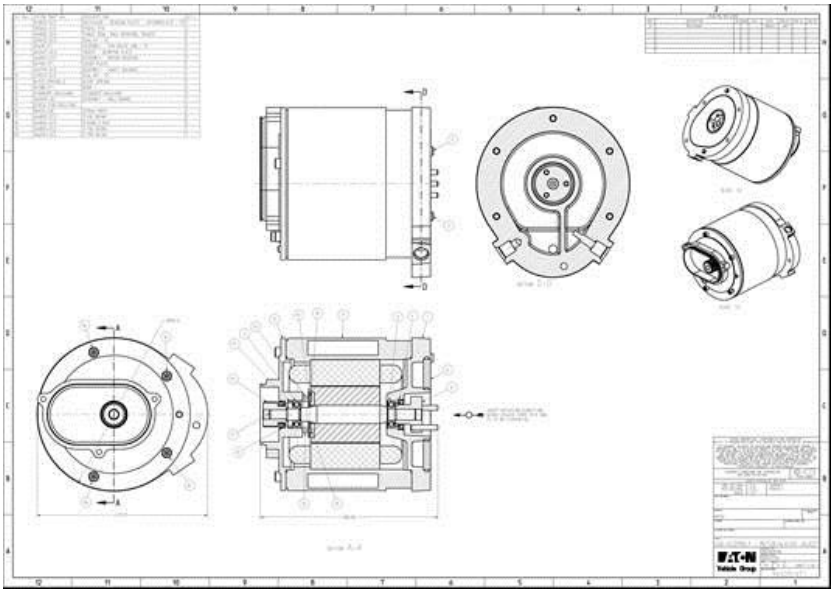

Figure 58: 12-turn Motor Layout

Figure 59 shows the motor and controller mounted on the dyno for testing.

Figure 59: 12-Turn Motor and Controller on Test

3.5.2 *Motor Testing*

Final testing on the 12-turn motor and controller resulted in the following performance maps. Figure 60 shows the efficiency map test results per the test plan specifications 3.1.3 & 12.2.2. The motor efficiency results are indicated by black lines and the electrical power supplied to the motor are indicated by red lines. Figure 61 also displays the motor efficiency map but the red lines represent the mechanical power, or shaft power, supplied by the motor, which will ultimately be the power supplied to the compressor/expander assembly.

$Power_{(in)} = Power_{(out)} + Motor\ Losses$

Volts x Current = Torque x rpm + Motor Losses

Where:

$Power_{(in)}$ = Red lines in Figure 60Figure 60

$Power_{(out)}$ = Red lines in Figure 61

This map includes the compressor/expander operational points which are mapped with the blue dotted line. The data shows that the motor is about 95% efficient at the top-end operating point (92 g/s flow rate, 2.5 bar) and drops down to ~75% efficiency at the 25% operating point (23 g/s flow rate, minimum 1.5 bar).

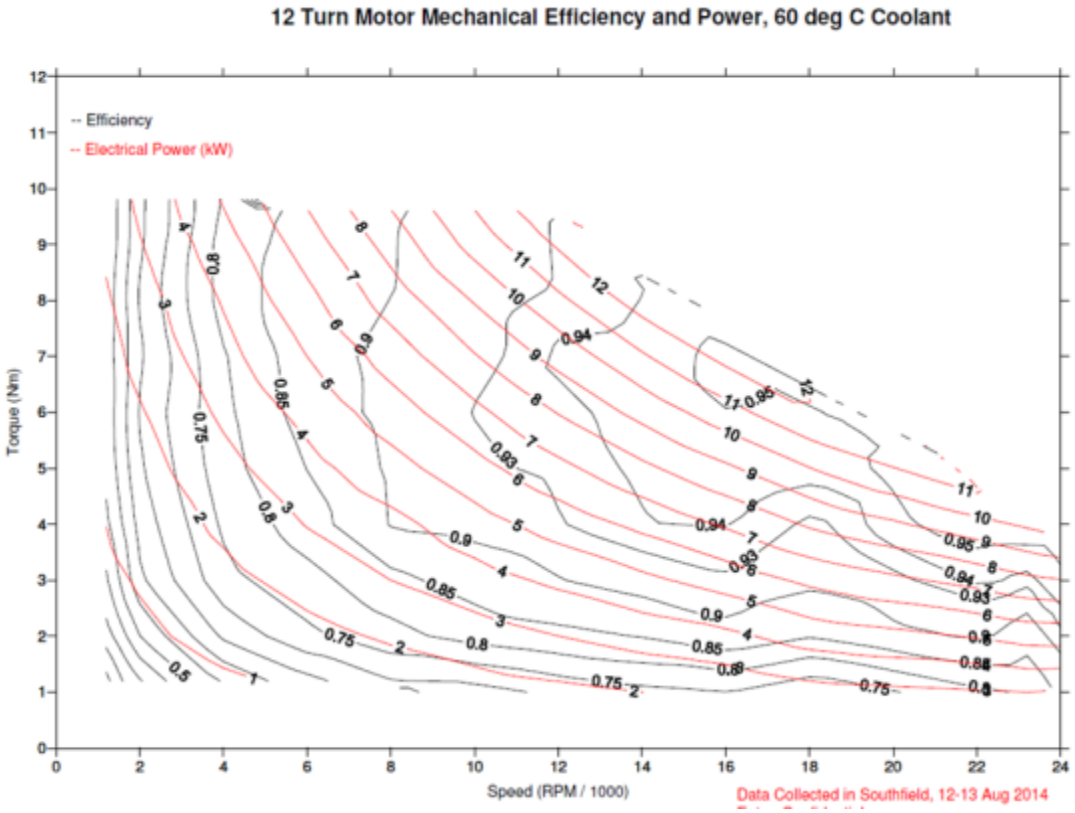

Figure 60: 12-Turn Motor and Controller $Power_{(in)}$ Map

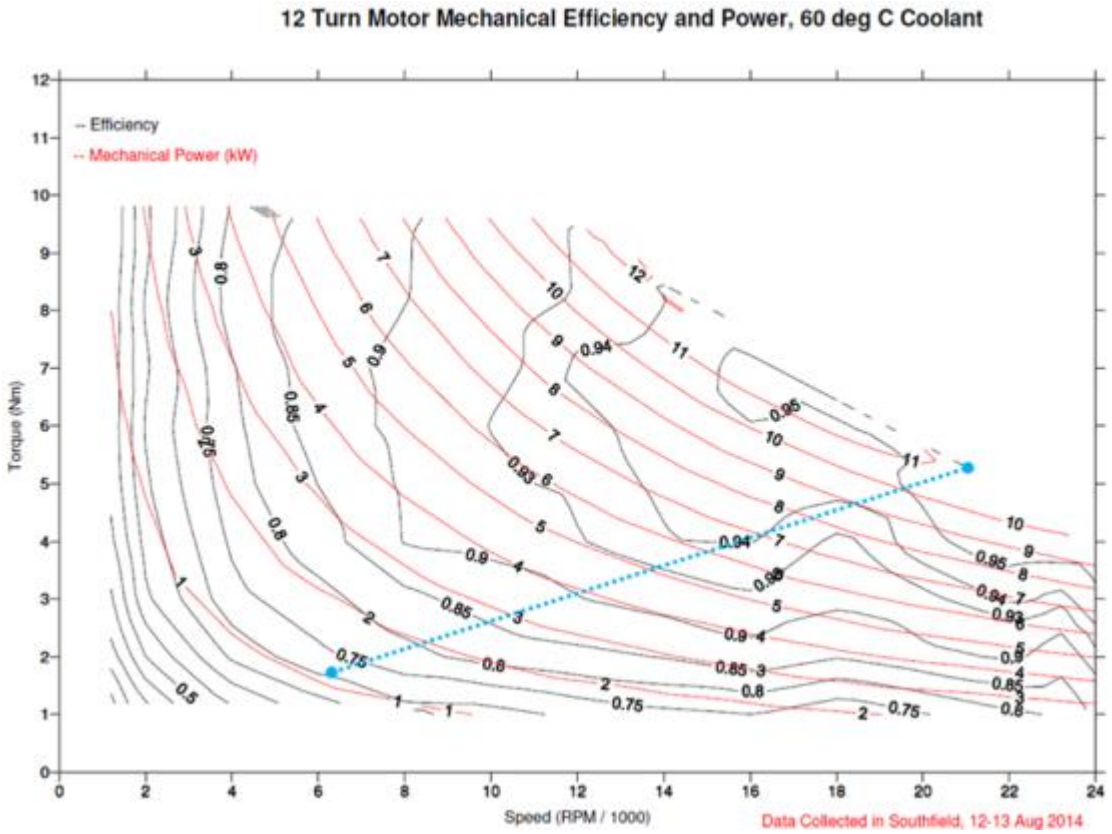

Figure 61: Motor Power$_{(out)}$ Map with Compressor Operation Zone Mapped

3.6 System Testing

3.6.1 *Approach*

Prior to testing the AMS as a complete sub-unit a study was conducted to determine the best way to test the unit in the lab. The strategy settled upon was an approach that tested the compressor and motor separate from the expander. This strategy was chosen because it presented the easiest means to control the compressor and expander and provide the best results.

Figures 62 and 63 outline the setups for the two separate tests. As a side note, prior to running these two tests, each of the individual components, compressor, motor and expander, were tested both under room/dry conditions and then the performance maps were adjusted to the specified operating conditions. When those tests were completed, the combined expander and a non-powered motor (the non-powered motor is included in order to obtain the motor and gearing parasitics in the expander mapping results), as shown in Figure 62, were tested together to obtain its combined performance maps. This setup was tested both at, dry and wet (wet is used to refer to the test being run at it specified relative humidity condition).

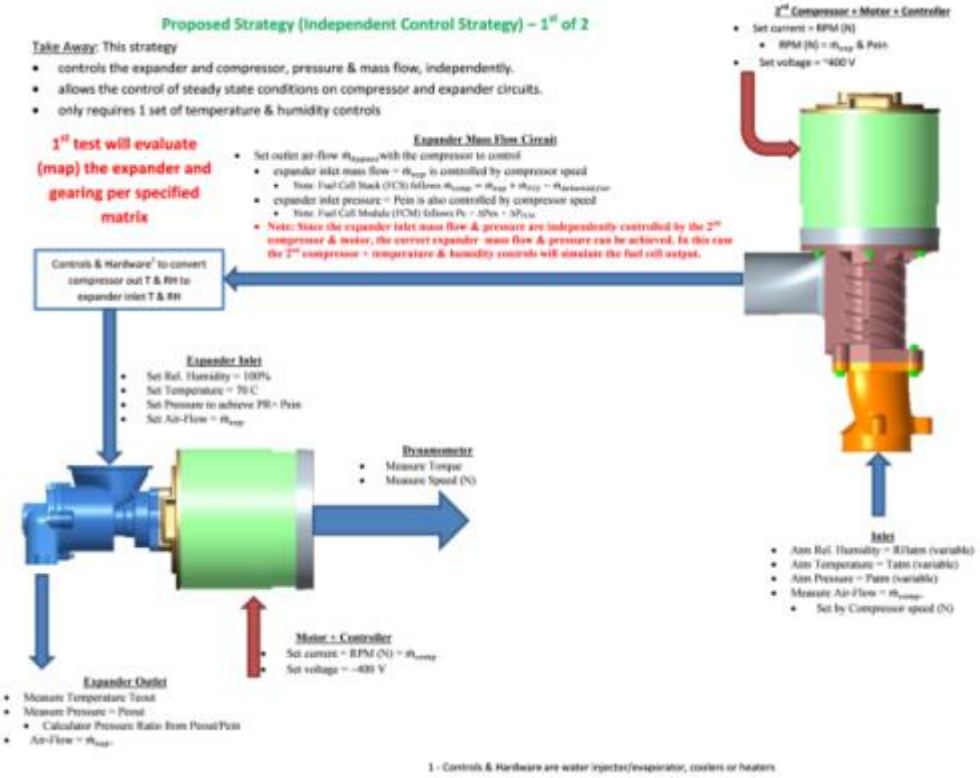

Figure 62: Independent Control Strategy A

After the expander map was created it was used as the input condition for the full system dynamometer test. This test combined the 12 turn motor with the V250 compressor and the supercharger dynamometer, as shown in Figure 63. The dynamometer was used as a motor to provide expander input power. The expander/motor maps generated in the first test was used as inputs to the motoring dynamometer which simulates the expander characteristics.

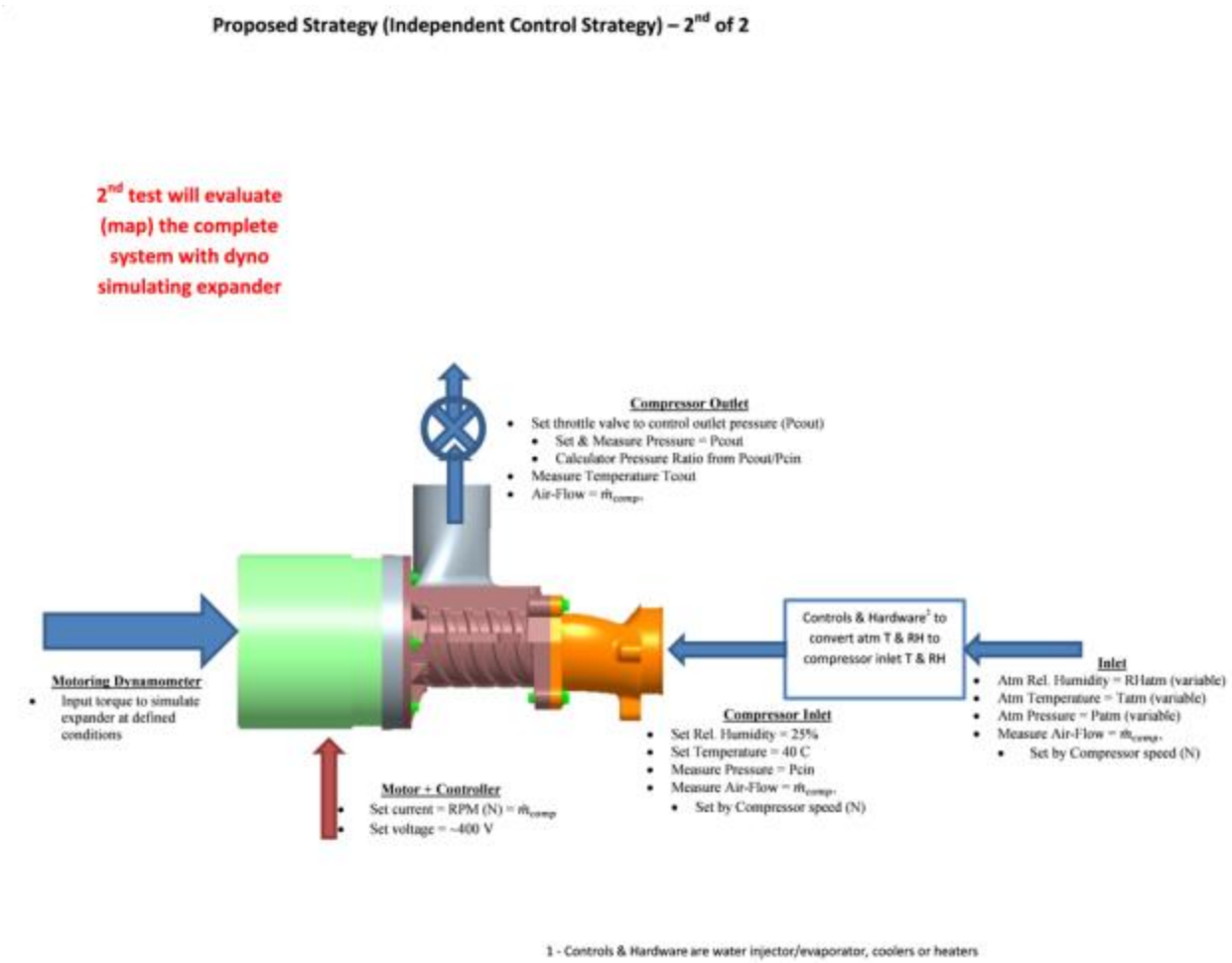

Figure 63: Independent Control Strategy B

3.6.2 *Expander Component Testing*

The expander was mounted to the dynamometer and pressurized air was supplied via an electric driven R410 compressor as shown in Figure 64.

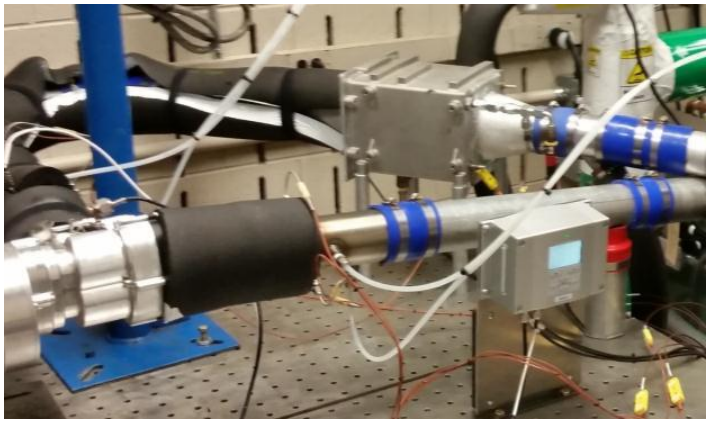

Figure 64: Dynamometer and Mounting Bench

The V210 expander tested was a 3-lobe, aluminum billet rotor expander. It was designed to operate at about half the speed of the compressor so that a larger, more efficient expander could be used.

For this test, the expander was mounted directly to the dynamometer and tested to “dry” test conditions. The inlet mass flow rate, inlet temperature, inlet pressure, outlet temperature, outlet pressure, speed and torque were monitored and recorded.

Figure 65 is the detailed map for the V210 expander. The expander efficiency results are shown by circular black lines. The output power of the expander is given by the angled red lines. The vertical green lines are the compressor speeds and the horizontal blue lines are the temperature differential of the air as it is expanded. The solid green line overlaid on the map is the 100%, 25% and idle operating points specified in the test plan. One can see that this expander has a fairly broad efficient range.

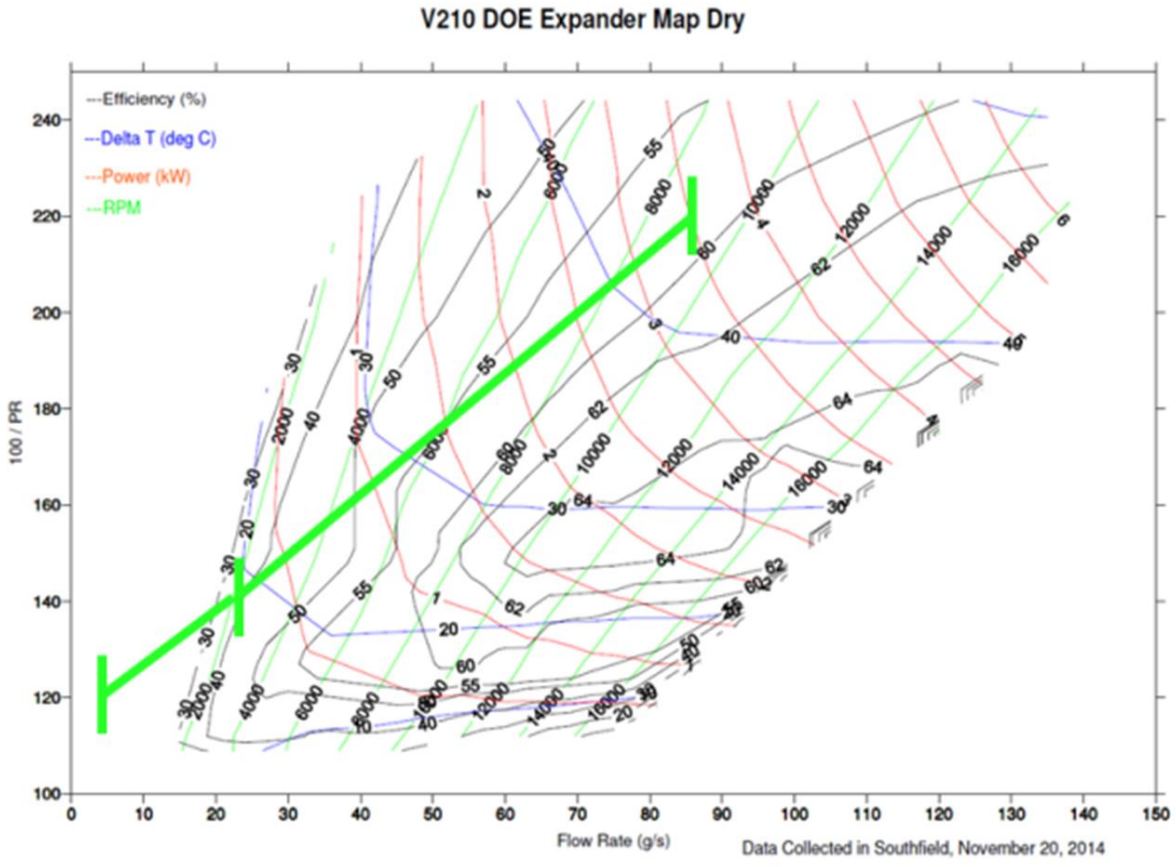

Figure 65: V210 Expander Map with Operating Points Mapped

Data for the 3 specified tests points, as tested, are as follow, derived from Figure 65 map:

	Mass Flow	PR	kW	RPM	Eff.	Delta Temp
100%	88	2.2	3.6	9200	58	-43
25%	23	1.4	0.32	2300	39	-20
Idle	4.6	<1.2	--	--	--	--

3.6.3 *Motor Component Testing*

Testing on the 12-turn motor & controller indicated that this motor configuration closely matched the V250 compressor speed range. The efficiency was greater than 95% for the 100% flow point and it only drops down to 75% efficiency at the 25% operating point.

Figures 66 and 67 are the efficiency maps for the motor and controller. Figure 66 shows the motor efficiency results (shown by black lines) and the electrical power supplied to the motor (shown by red lines). Figure 67 is also the motor efficiency map but the red lines are the mechanical power, or shaft power, supplied by the motor (this will be the power supplied to the compressor/expander assembly).

For reference, Figure 66 is the performance map of the motor with the electrical power supplied to the motor or $Power_{(in)}$. Figure 67 is the performance map of the motor with the mechanical power coming out of the motor, shaft power, or $Power_{(out)}$. Below is the equation showing the relationship between the two maps

$Power_{(in)} = Power_{(out)} + Motor\ Losses$

$Power_{(in)} = Volts \times Current$

$Power_{(out)} = Torque \times rpm$

or

$Volts \times Current = Torque \times rpm + Motor\ Losses$

Where:

$Power_{(in)}$ = Red lines on Figure 66 graph

$Power_{(out)}$ = Red lines on Figure 67 graph

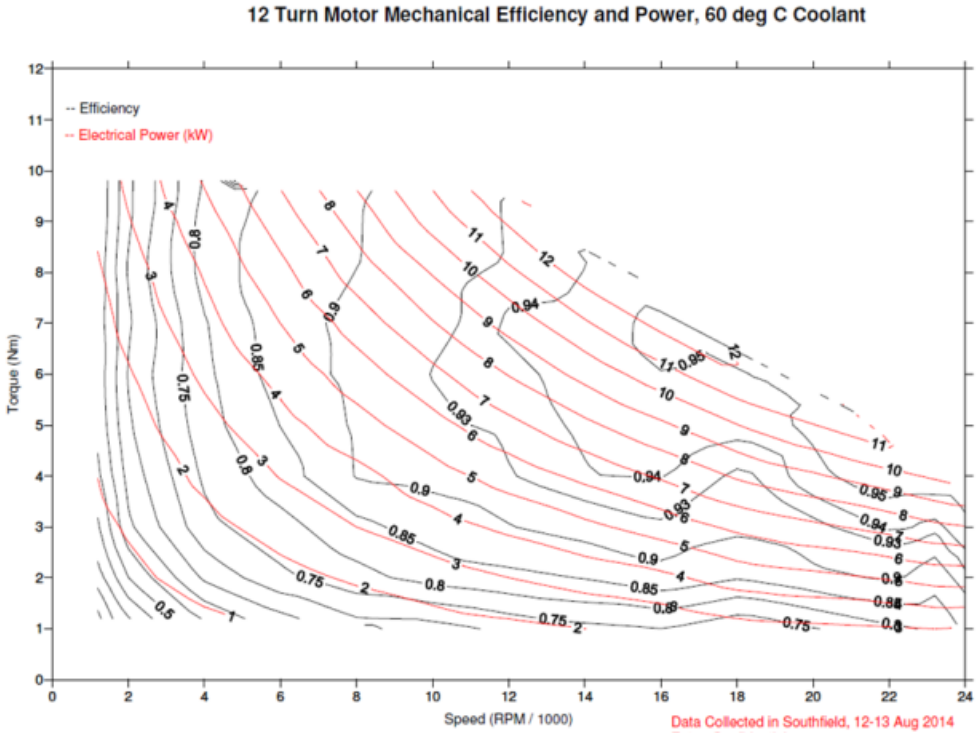

Figure 66: 12-Turn Motor and Controller $Power_{(in)}$ Map

.

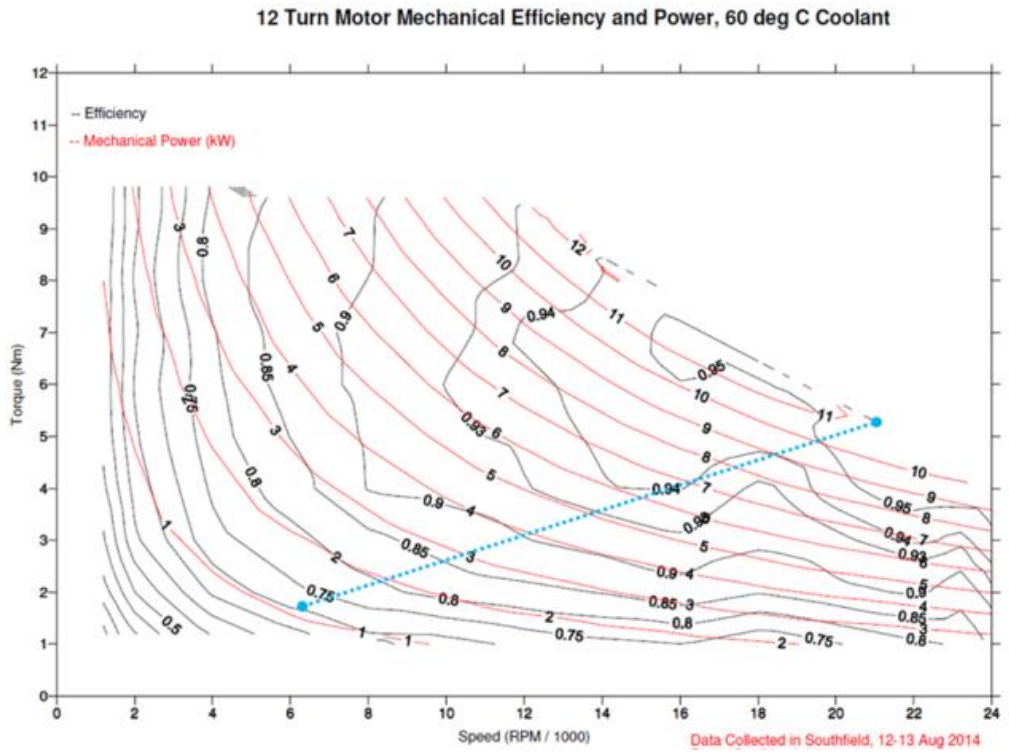

Figure 67: Motor Power$_{(out)}$ Map with Compressor Operation Zone Mapped

3.6.4 *Compressor Component Testing*

The V250 compressor tested is a 3-lobe, aluminum billet rotor compressor. It was designed to have the highest efficiency island located in the mid-speed operating range. The reason for placing the efficiency at this location was so that the maximum compressor efficiency would be located where the fuel cell operated the most. If the maximum operating range was located at maximum power point (i.e., 100% flow), then an alternative compressor would have been chosen.

For this test, the compressor was mounted directly to the dynamometer. The inlet mass flow rate, inlet temperature, inlet pressure, outlet temperature, outlet pressure, speed and torque were monitored and recorded. A back pressure valve controlled the exhaust air from the compressor for the purpose of controlling the compressor pressure ratio. Figure 68 is the compressor mounted to the motor.

Figure 69 is the detailed map for the V250 compressor. The compressor efficiency results are shown by circular black lines. The input power to the compressor is given by the angled red lines. The vertical green lines are the compressor speeds and the horizontal blue lines are the temperature increase of the air as it is compressed. The solid green line overlaid on the map is the 100%, 25% and idle operating points specified in the test plan.

One can see that this compressor has a fairly broad efficient range. The compressor efficiency is greater than 66% between 35% flow and 80% flow. This provides good overall operating performance for a fuel cell application that has a broad operating range.

The map shows that the V250 compressor has a power requirement of 14.8 kW, an efficiency of 59%, a maximum temperature of 166C and an operating speed of 22000 rpm at the 100% flow

point (92 g/s flow rate, 2.4 bar). At the 25% operating point (23 g/s flow rate, minimum 1.5 bar) the power requirement drops to 1.4 kW, the efficiency raises to 63%, the temperature drops to 86C at an operating speed of 6000 rpm. When the compressor performance is evaluated to idle the power required is 230 watts, the efficiency is 56%, the operating temperature is 60C and the operating speed is 2000 rpm.

	Mass Flow	PR	kW	rpm	Eff.	Delta Temp
100%	92	2.4	14.8	22000	59%	166C
25%	23	1.5	1.4	6000	63%	86C
Idle	4.6	1.2	0.23	2000	56%	60C

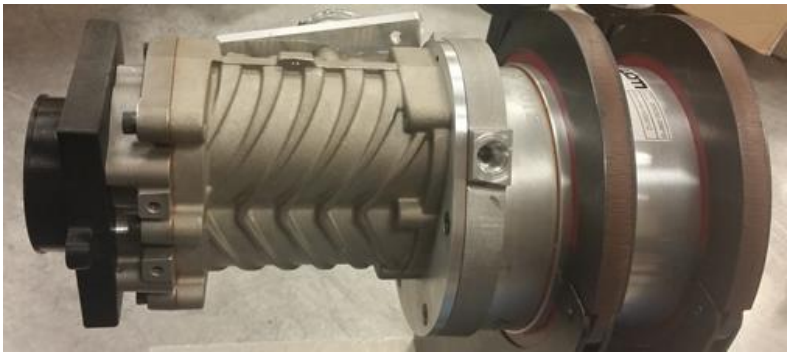

Figure 68: V250 Compressor

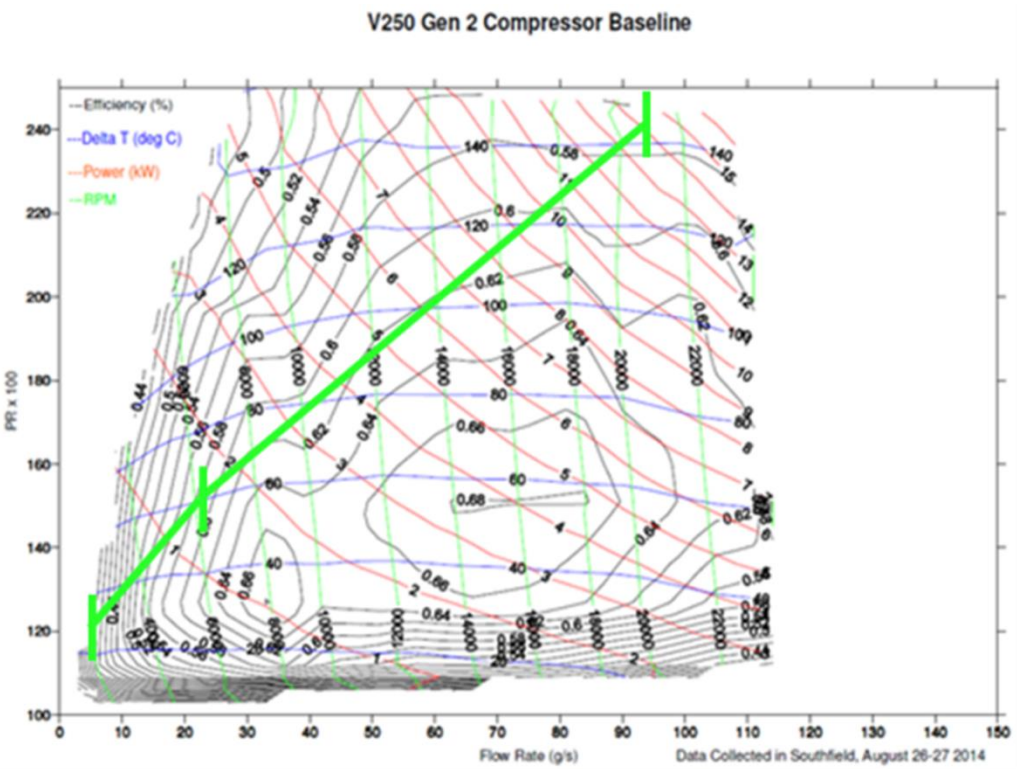

Figure 69: V250 Compressor Map with Operating Points Mapped

3.6.5 *Sub-System Testing – Expander + Motor*

The V210 expander was attached to the 12 turn motor and then mounted to the dynamometer as shown in Figure 70. Pressurized air was supplied via a driven compressor. The expander inlet air was temperature and humidity controlled. The exhaust air is vented to atmospheric pressure via room exhaust vent.

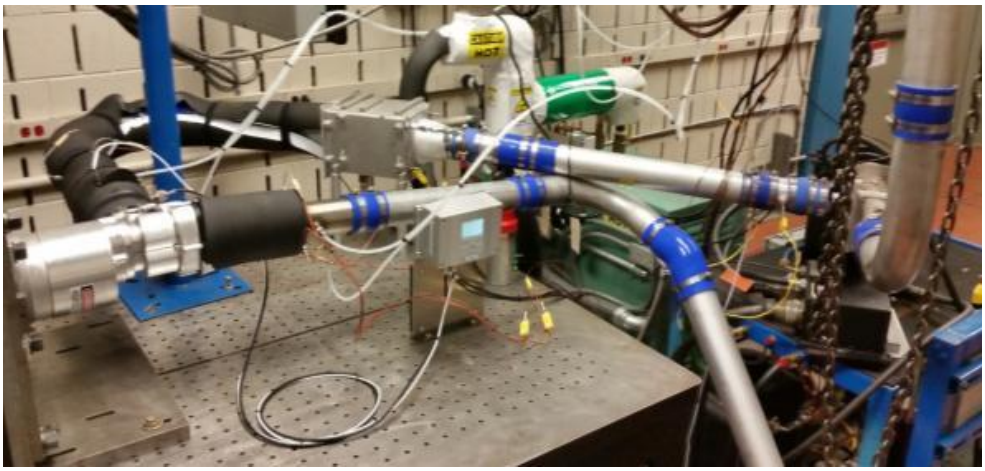

Figure 70: Dynamometer & Mounting Bench

The results with the V210 expander with motor are shown in Figure 71. As with the other maps, this map follows the same color line, output parameter relationship. The solid green line overlaid on the map is the 100%, 25% and idle operating points specified in the test plan.

Figure 71 is the map for the relative humidity test performed on the V210 expander attached to the motor. The tests were completed in accordance to the published test plan. This test did not power the motor during the mapping process. Its purpose of inclusion was to obtain a combined map with the step-up gear and parasitic losses.

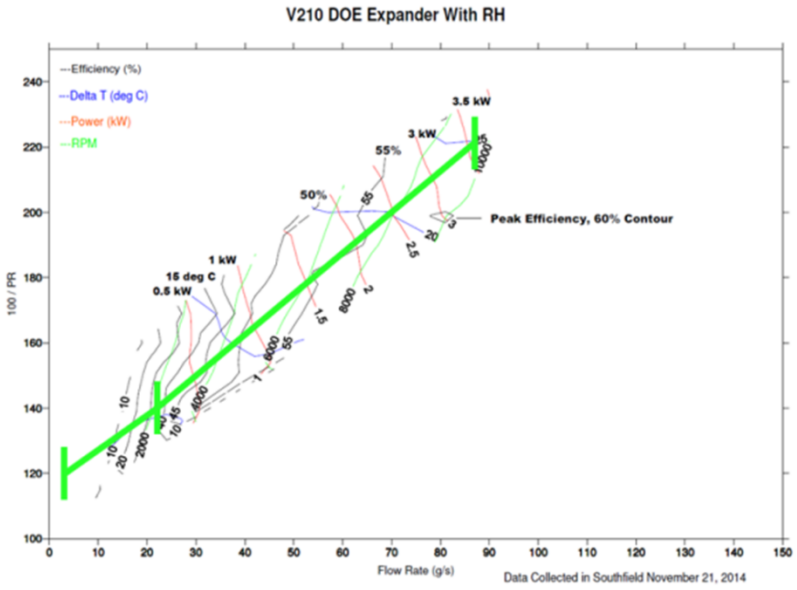

Figure 71: The V210 Expander + Motor Results (Wet)

The map shows that the V210 expander + motor produced less power than the expander alone, which is expected. Adding the motor introduces more parasitic losses driving down the power output and the overall efficiency.

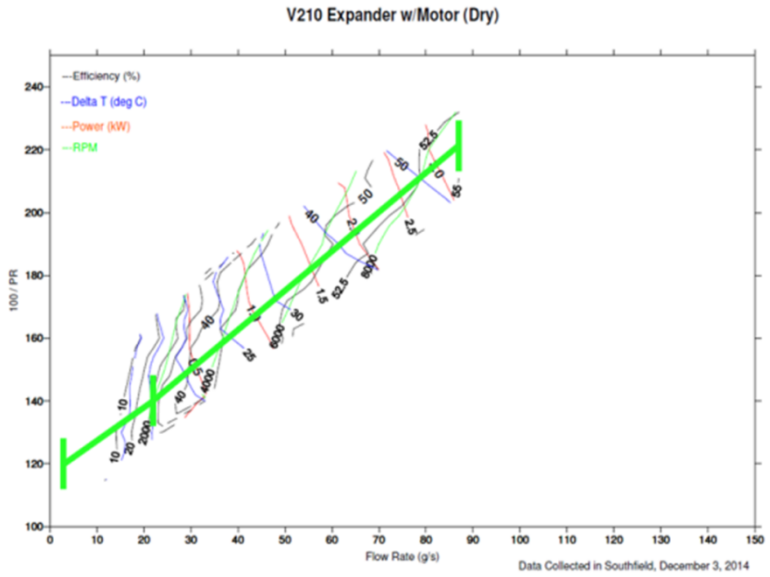

Figure 72: The V210 Expander + Motor Results (Dry)

The combined expander and motor tested with dry conditions reduces the power output when compared to the humidity tests. Figure 72 shows a partial map similar to the humidity test shown in Figure 71.

3.6.6 *Full-System Testing – Dynamometer + Motor + Compressor*

The full-system test is designed to prove that the power generated by the expander provides an equal reduction in power consumption at the motor controller. For the test, the V250 compressor and 12 turn motor were mounted to the supercharger dynamometer. The combined expander and motor (wet) data was used as an input to the dynamometer to simulate the expander power. The compressor inlet air temperature was controlled. The inlet mass flow rate, inlet temperature, inlet pressure, outlet temperature, inlet pressure, speed, motor current and voltage were measured. A back pressure was utilized in order to control the compressor pressure ratio. The compressor exhaust was then vented to atmospheric pressure via room exhaust vent.

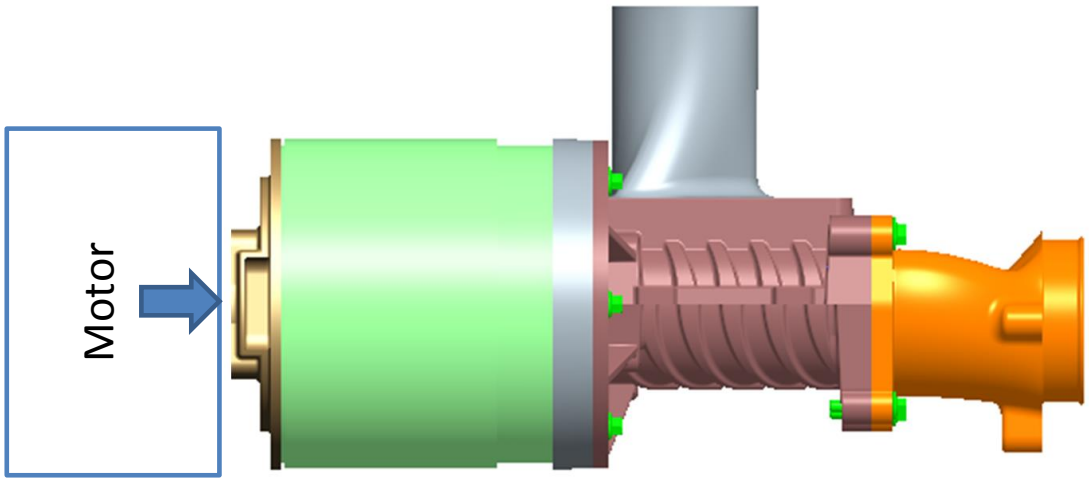

Figure 73: Motor + 260 Compressor

Figure 73 shows the layout of the full system test components with the dynamometer driving the motor in place of the expander. Figure 74 shows the actual test setup with the motor and compressor mounted to the dyno.

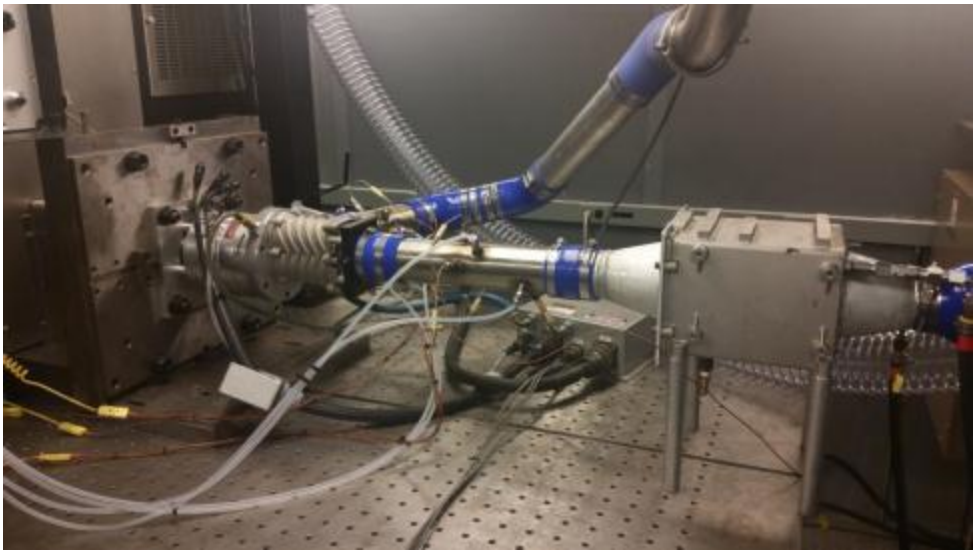

Figure 74: Full System Test with Motor and Compressor Mounted to the Dyno

The results of this test indicate that the mechanical power produced by the expander directly translates into electrical power saved at the system level. The results are shown in the table below.

Table 8: Total System Power with and without Expander

System Power Without Expander			
	System Mass Flow @ Comp.	PR @ Comp.	kW_e
100%	92	2.4	**15.5**
25%	23	1.5	**1.9**
Idle	4.6	1.2	**0.4**
System Power With Expander			
	System Mass Flow @ Comp.	PR @ Comp.	kW_e
100%	92	2.4	**12.1**
25%	23	1.5	**1.6**
Idle	4.6	1.2	**0.4**

It must be noted that because there is a pressure and flow rate change between the air flow entering and exiting the fuel cell, the compressor and expander operate at different speeds and pressures. The power produced by the expander is directly influenced by the components of the fuel cell that are before it in the system. Thus, a correlation method must be determined in order to match the compressor operating point to the expander operating point.

The method used to correlate the compressor and expander operating points is critical for accurate determination of the actual power consumed by the system at a given point. The test matrix for this test was created by selecting speed and pressure ratio data points from the expander + motor (wet) test. To determine the data points of the compressor + motor test to capture, the speed of the expander was multiplied by the gear ratio for each point and the pressure ratio was increased by 10% to account for the pressure losses through the fuel cell. To more accurately determine total system power consumption during operation, the pressure losses through the fuel cell should be characterized.

3.6.7 *Full-System Noise Testing*

The AMS was tested in Eaton's acoustic dynamometer room. Figure 75 is a picture of the setup. A sound pressure transducer was placed about 1 meter from the AMS to measure the noise level. There were 3 tests run to see how Eaton's noise abatement structure effectively reduced AMS noise. The first test conducted included a noise deadening enclosure with noise dampening material that enclosed the compressor. This test measured 95.6 dB(a) at full flow. The second test had the noise deadening enclosure removed but the noise dampening material remained attached to the compressor. The test saw an increase sound level of 2.7 dB(a) and results measured were 98.3 dB(a). The last test had all the noise abatement removed and measured a 100.4 dB(a), a 2.4 dB(a) increase.

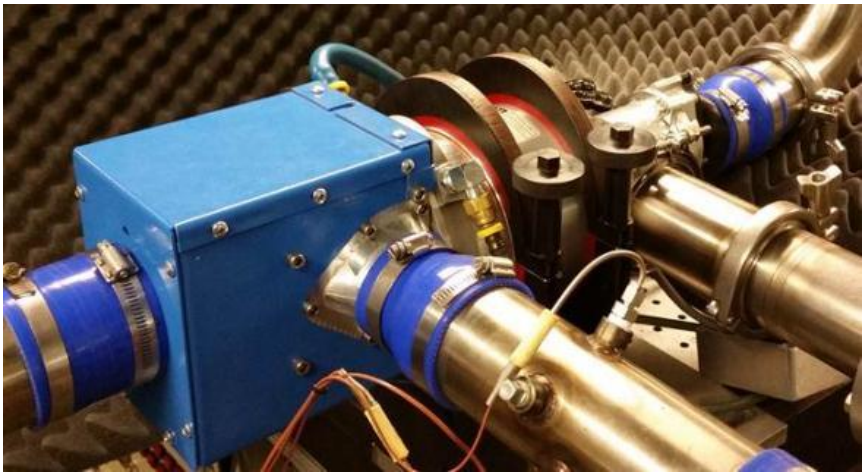

Figure 75: Noise Measurement Test Setup

3.6.8 *Transient Time Testing*

The AMS was easily able to accelerate from 10% flow to 90% flow in one second due to the high power capability of the motor. It took about 3.5 kilo-joules to accelerate the AMS in one second. Figure 76 presents the time dependent results.

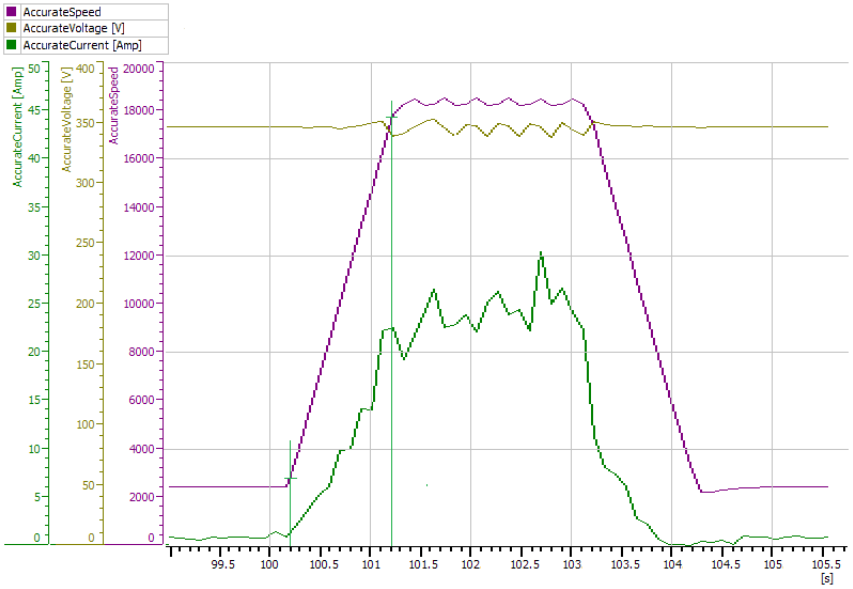

Figure 76: Compressor, Motor & Expander Acceleration Time Results

The test was set up with the compressor outlet ported to the expander inlet and the expander outlet ported to room air, see Figure 77. Before the test was run, the rpm values which correspond to the 10% and 90% flow points (10% = 9.2 g/s & 90% = 82.8 g/s) were determined. These rpm points were programed into the controller, the controller voltage was set to 350 V_{dc} and the test stand was programmed to supply the appropriate current to accelerate the motor from the 10% flow point to the 90% flow point in one second. The compressor inlet and outlet pressure, inlet and outlet temperature & speed, power supply output, and mass flow were monitored.

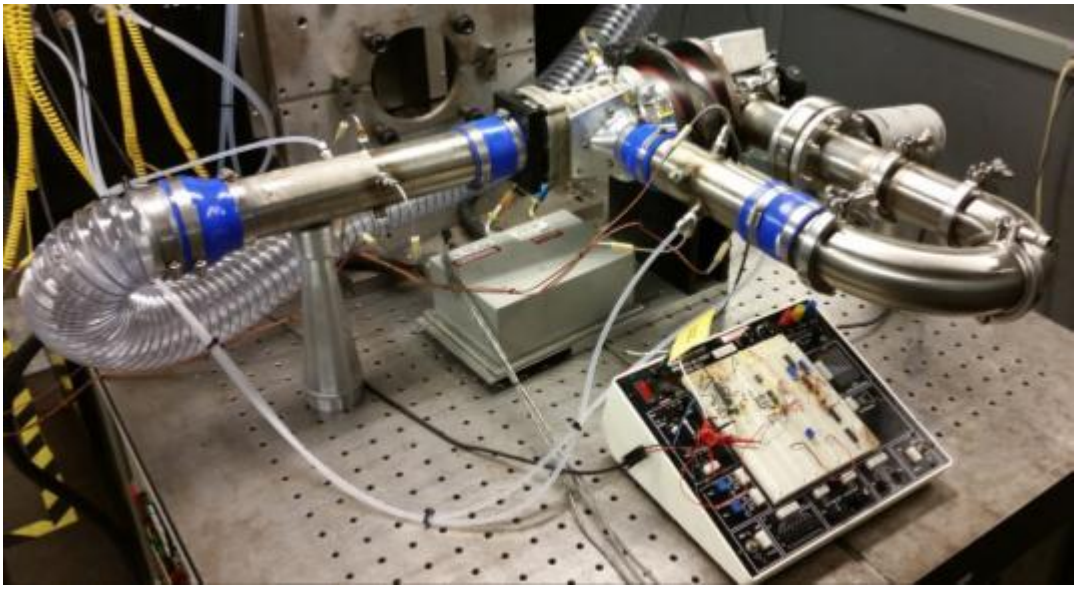

Figure 77: AMS Acceleration Test Setup

3.7 HD7 Fuel Cell Testing

3.7.1 *Objective*

The objective for the work done by Ballard was to assess the performance of Eaton's new compressor/ expander air delivery system on Ballard's HD7 fuel cell system. This will require bench marking the HD7 fuel cell performance with our baseline air delivery system, then test the HD7 system with Eaton's new compressor/ expander air delivery system.

3.7.2 *Executive Summary*

Testing at Ballard was completed over 14 months from February 2015 to March 2016 using two Eaton compressor/expander air delivery systems on two different Ballard test stations. System 1 was used for setup and software testing for integration into the Ballard HD7 module as well as water injection testing. Unit 2 was used for assessment when integrated with the Ballard module to compare with the incumbent Ballard air delivery system.

In addition to the assessment of the compressor the following work was also completed as part of this project.

- Automated data collection using Matlab
- Transmission of test data to ANL for use in a fuel cell/compressor model
- Water injection testing to the compressor inlet as a possible method of reducing complexity of future fuel cell modules.

3.7.3 *Background*

3.7.3.1 Objective

Testing was performed to assess a new air system provided by Eaton for use with the HD7 module, Ballard's next generation heavy duty fuel cell system. The overall purpose of the testing was to determine the performance (efficiency) benefits of the Eaton air management system that incorporates an exhaust expander.

Fuel cells run with pressurized air, in some cases there is excess pressure and energy in the exhaust stream of the fuel cell. This series of tests investigated the advantage of using higher pressurized inlet air and the recapturing of the higher exhaust pressure that is a result of the higher inlet pressure. Figure 78 below shows the Eaton compressor/expander setup with HD7 heavy duty module.

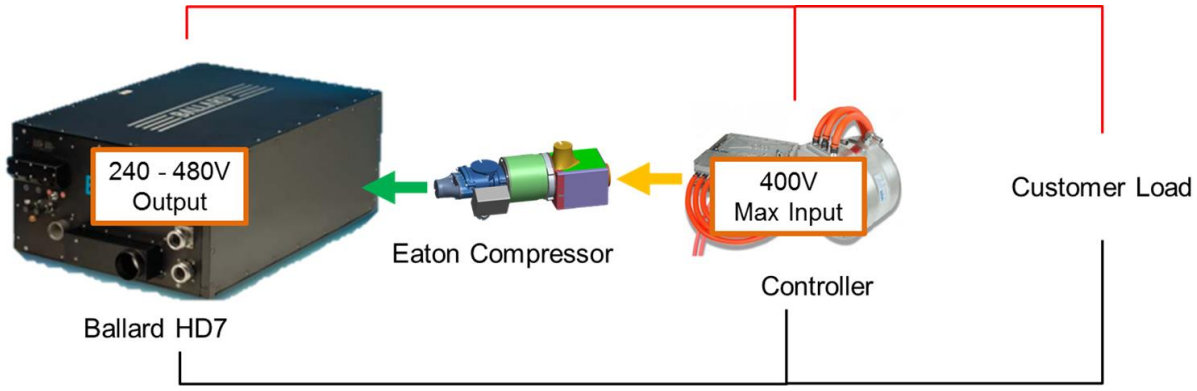

Figure 78: Test Setup

3.7.3.2 Test Plan

The following diagram illustrates the test plan for the two Eaton compressors with expander units.

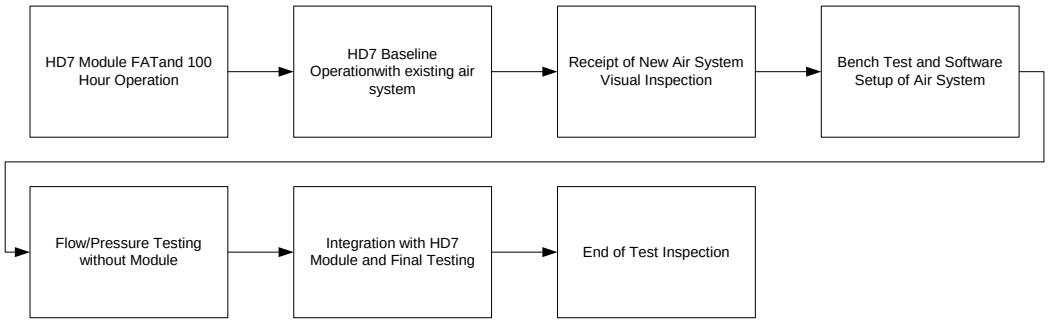

Figure 79: Testing Flow Chart

3.7.4 *Results and Discussion*

3.7.4.1 Parameters recorded and Argonne National Laboratories Co-operation

The following parameters were recorded for each test and the data shared with ANL for their model development activities.

- Actual percent power (%)
- Stack Current (Amps-DC)
- Stack Voltage (Volts-DC)
- Stack Gross Power (kW)
- Cathode mass flow (gps)
- Compressor outlet temperature (°C)
- Cathode in Humidifier in temperature (°C)
- Stack Ox inlet temperature (°C)
- Stack Ox outlet temperature (°C)
- Stack Fuel inlet pressure
- Stack Coolant inlet temperature
- Stack coolant outlet temperature

- Module coolant inlet temperature
- Module coolant outlet temperature
- Cathode Out Humidifier out temperature (°C)
- Compressor out/Aftercooler in pressure (barg)
- Humidifier in pressure (barg)
- Stack Ox in pressure (barg)
- Stack Ox outlet pressure (barg)
- Humidifier shell outlet pressure (barg)
- Compressor current draw (A)
- Compressor power draw(Calculated from compressor current draw and stack voltage)
- Compressor speed(RPM)

Data from all test configurations were shared and analysed by ANL. Their data and results are not part of this report.

3.7.4.2 Baseline Testing

The HD7 system was operated using the existing air system. The load profile used was a combination of down-polarizations, up polarizations, constant current operation, and several cycles of the “Whistler Drive Cycle”, which is a dynamic load profile taken from field data. The entire baseline test lasted for approximately 3 days. The current drawn from the system as a function of time is shown in Figure 80 below.

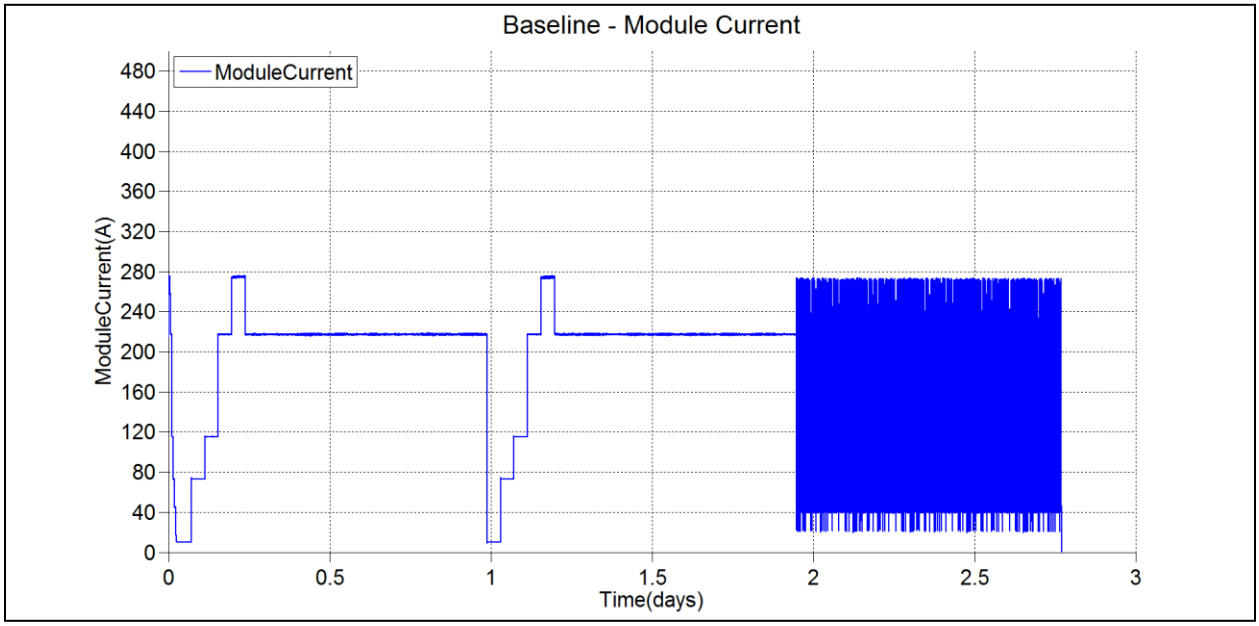

Figure 80: Baseline Testing - Module Current

During testing, a data acquisition system logs process parameters internal to the module. These include stack specific parameters, including voltage and current, as well as air system specific parameters, including flows, temperatures and pressures measured throughout the air system.

Figure 81 to Figure 86 below provide a graphical representation of a sample of the data collected.

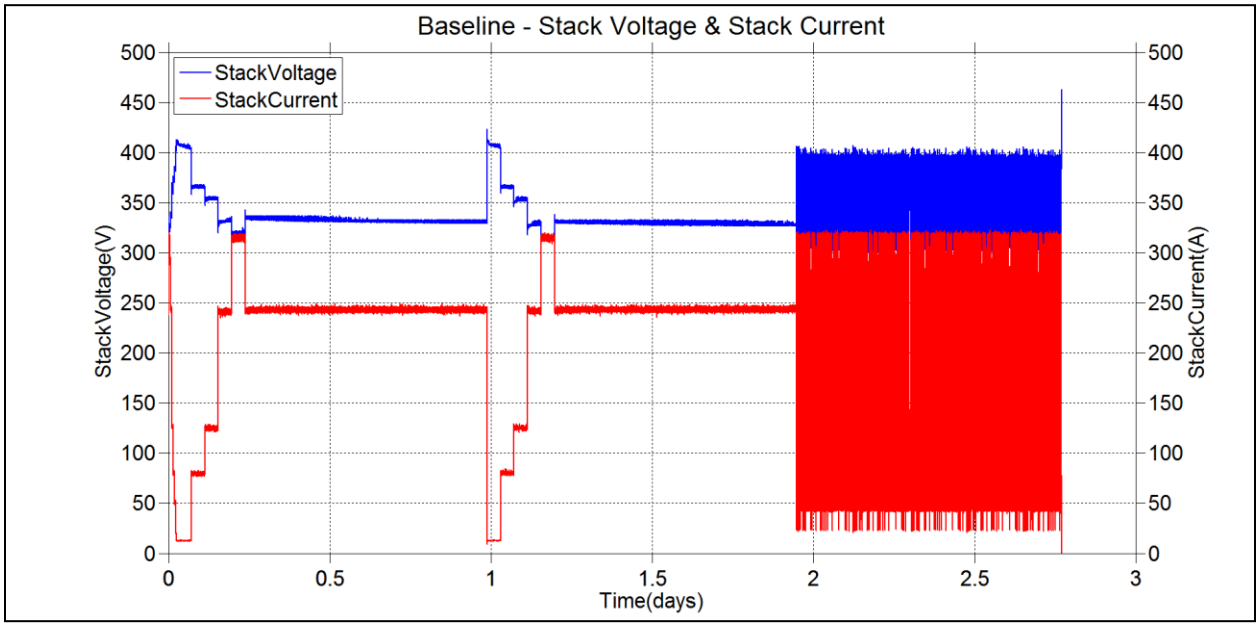

Figure 81: Baseline Testing - Stack Current and Voltage

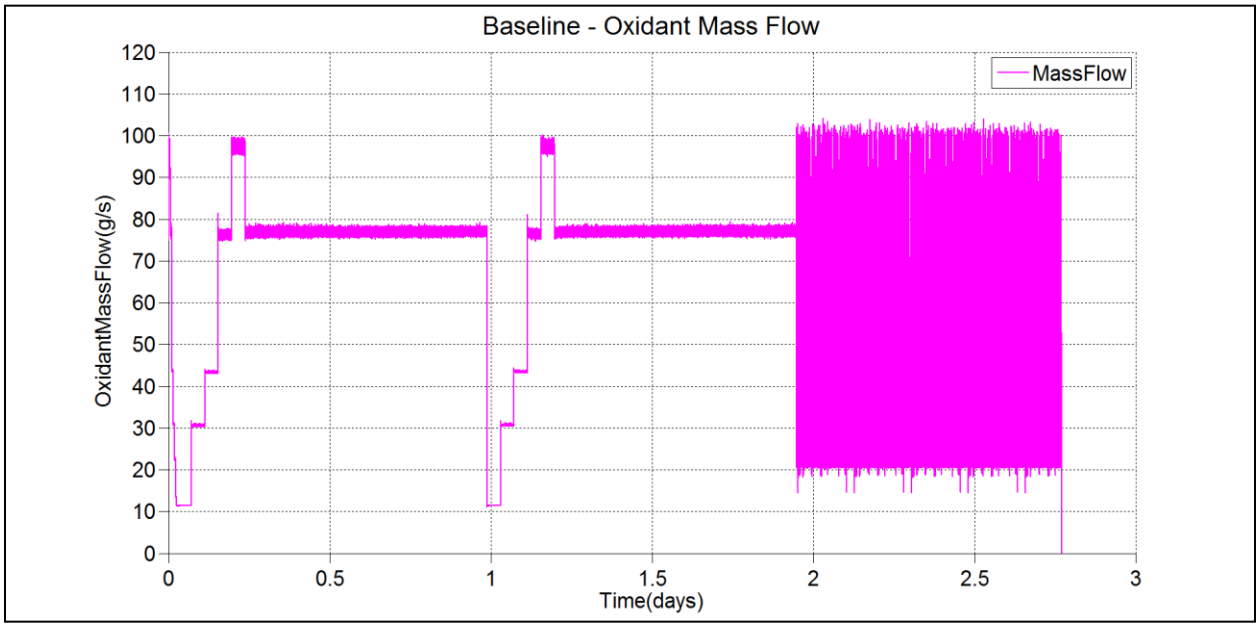

Figure 82: Baseline Testing - Oxidant Mass Flow

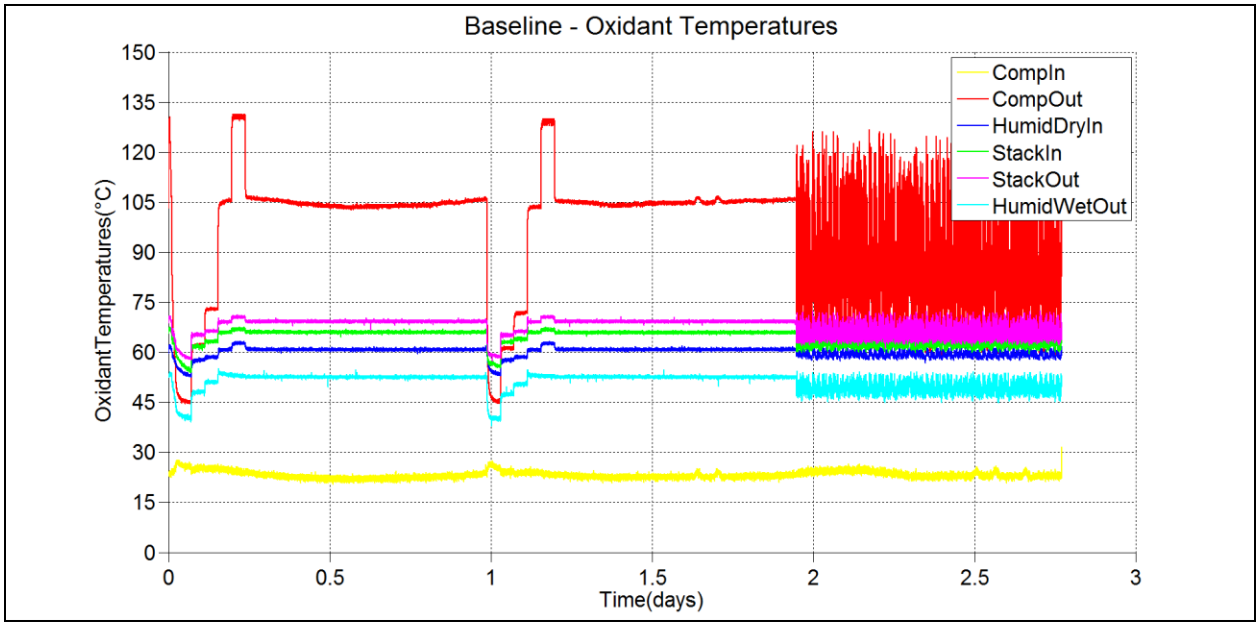

Figure 83: Baseline Testing - Oxidant Temperatures

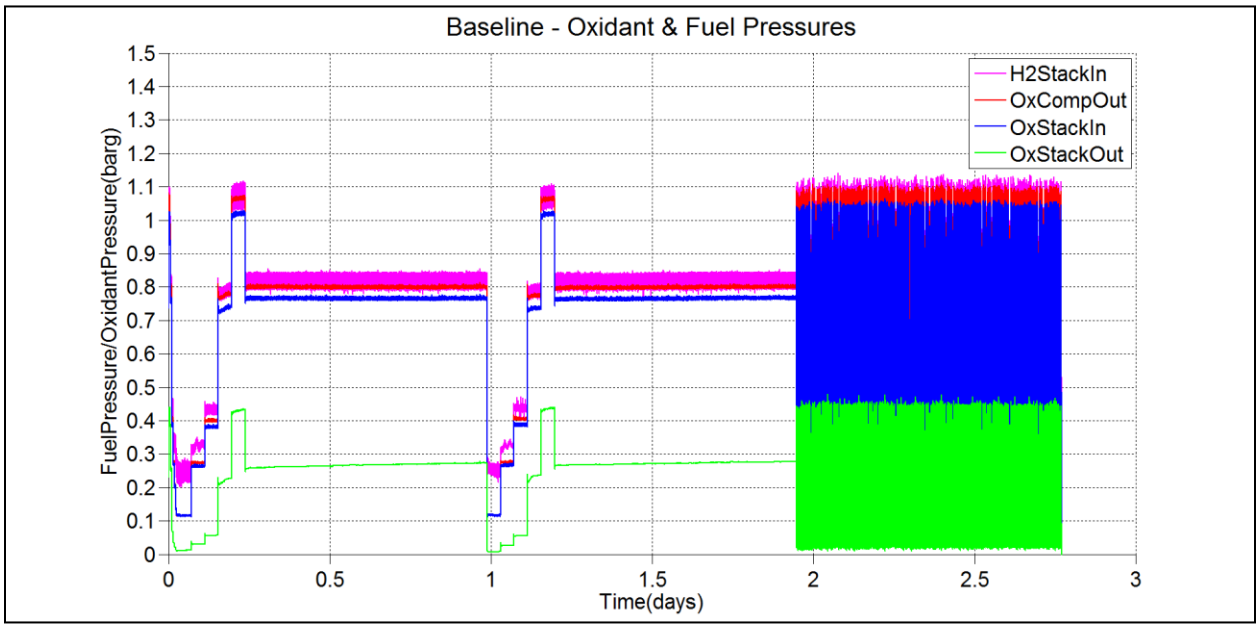

Figure 84: Baseline Testing - Oxidant and Fuel Pressures

Additionally, the compressor current and power were also logged, as shown in the below figures. The data collected can be used to directly compare the performance of the existing system with Eaton's Air Management System, including operation with the expander.

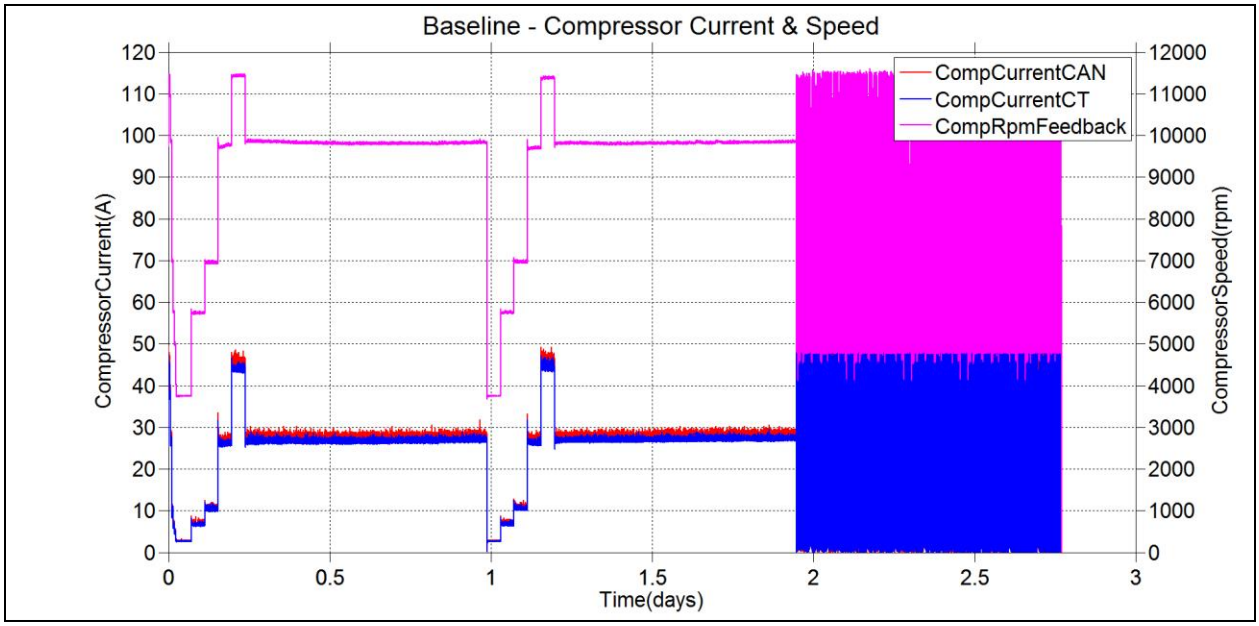

Figure 85: Baseline Testing – Compressor Current and Speed

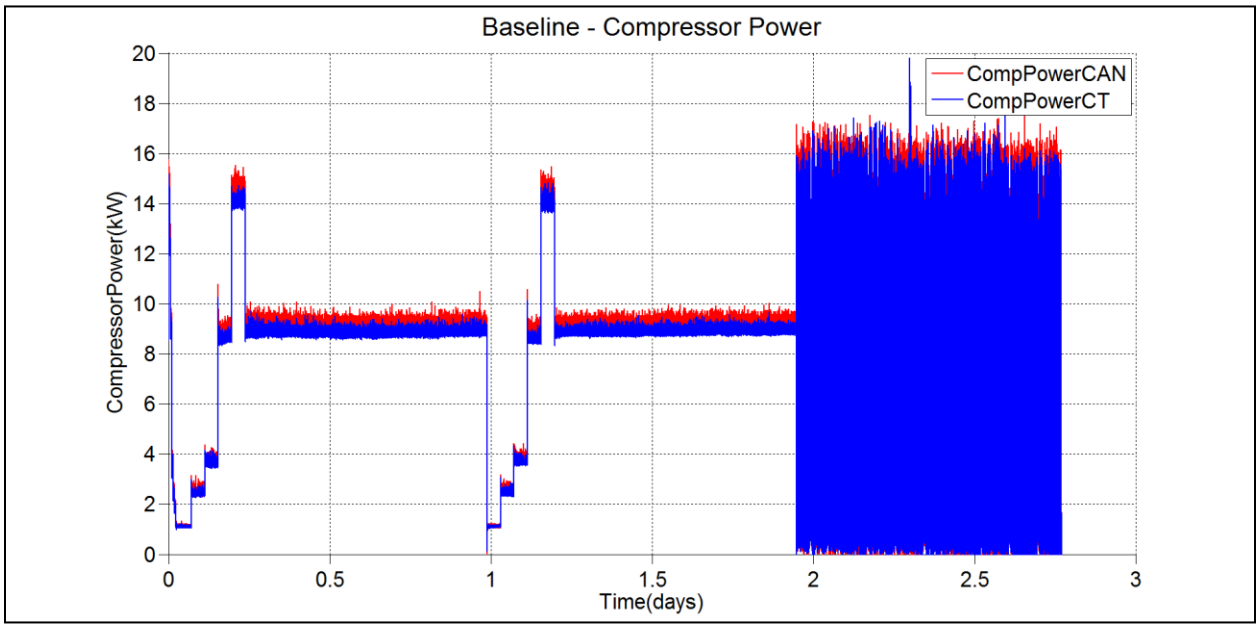

Figure 86: Baseline Testing – Compressor Power

The performance of the incumbent air delivery system with the Ballard HD7 fuel cell module (FCM) had an efficiency of 48.1% LHV H2 at the 240A fuel cell stack steady state operating point of 220A Fuel Cell current.

LHV Efficiency = Net Power (kW) / (fuel flow(g/s)) LHV constant (120.0412 kJ/g for hydrogen))*
Equation 1: LHV efficiency Calculation

3.7.4.3 Eaton Compressor/Expander Testing

3.7.4.3.1 Integration

Integration of the Eaton compressor/expander system with the HD7 fuel cell was successfully completed as depicted in Figure 87.

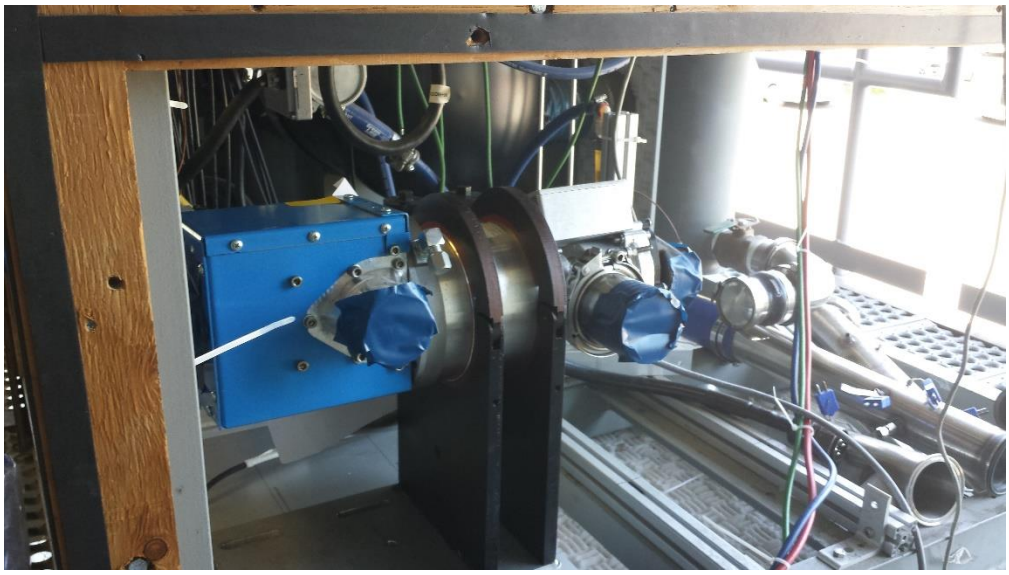

Figure 87: Eaton Air Management System Partially Installed in Ballard's compressor test stand.

3.7.4.3.2 Eaton Compressor Only in Configuration 1

Mechanically, the existing air-kit was removed, and a new air-kit was developed, based around the Eaton system. The compressor and controller were both packaged into the new air kit, and the oxidant plumbing was re-worked to accommodate. Also, a coolant loop was incorporated to controller. Test 1 was to test the compressor only with the expander removed based on the diagram shown in Figure 88.

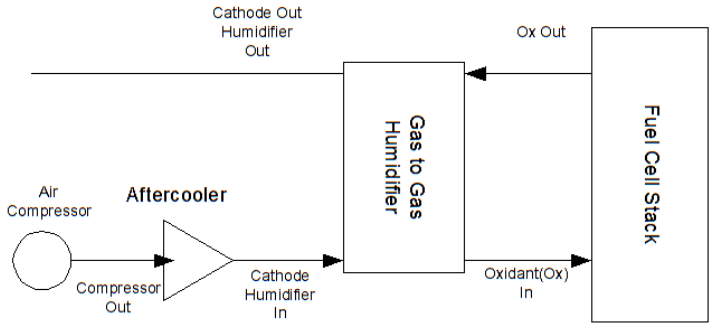

Figure 88: Configuration 1 Setup

The load profile used was a combination of down-polarizations, up polarizations, constant current operation, and several cycles of the “Whistler Drive Cycle”, which is a dynamic load profile taken from field data. The entire test lasted for approximately three days.

During testing, a data acquisition system logged process parameters internal to the module. These include stack specific parameters, including voltage and current, as well as air system specific parameters, including flows, temperatures and pressures measured throughout the air system.

The entire baseline test lasted for approximately three days. The current drawn from the system as a function of time is shown in Figure 89

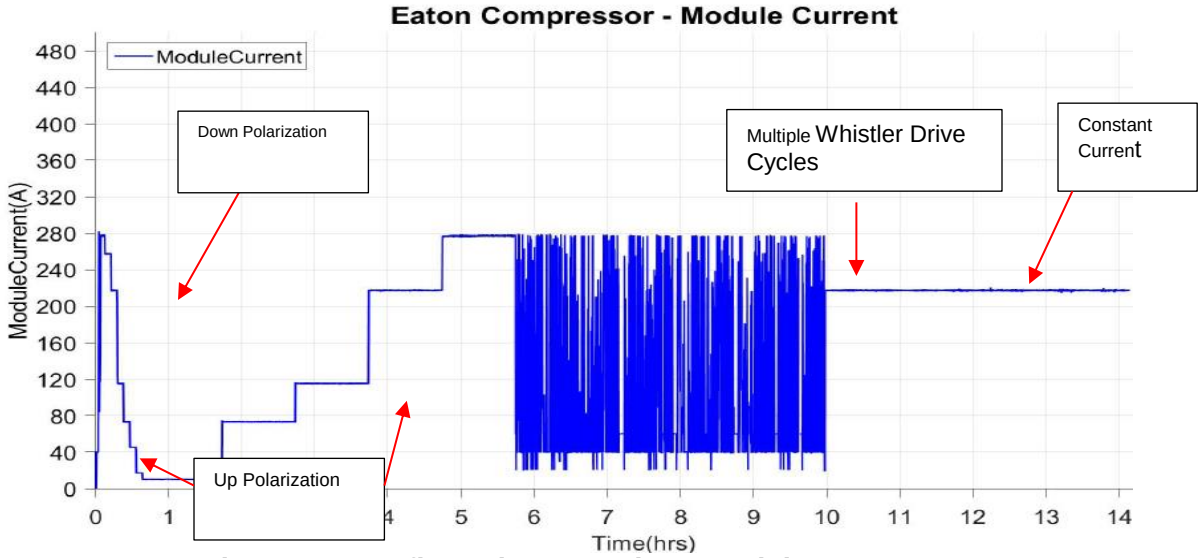

Figure 89. Configuration 1 Testing - Module Current

During testing, a data acquisition system logged process parameters internal to the module. These include stack specific parameters, including voltage and current, as well as air system specific parameters, including flows, temperatures and pressures measured throughout the air system. Figure 90 through Figure 93 provide a graphical representation of a sample of the data collected.

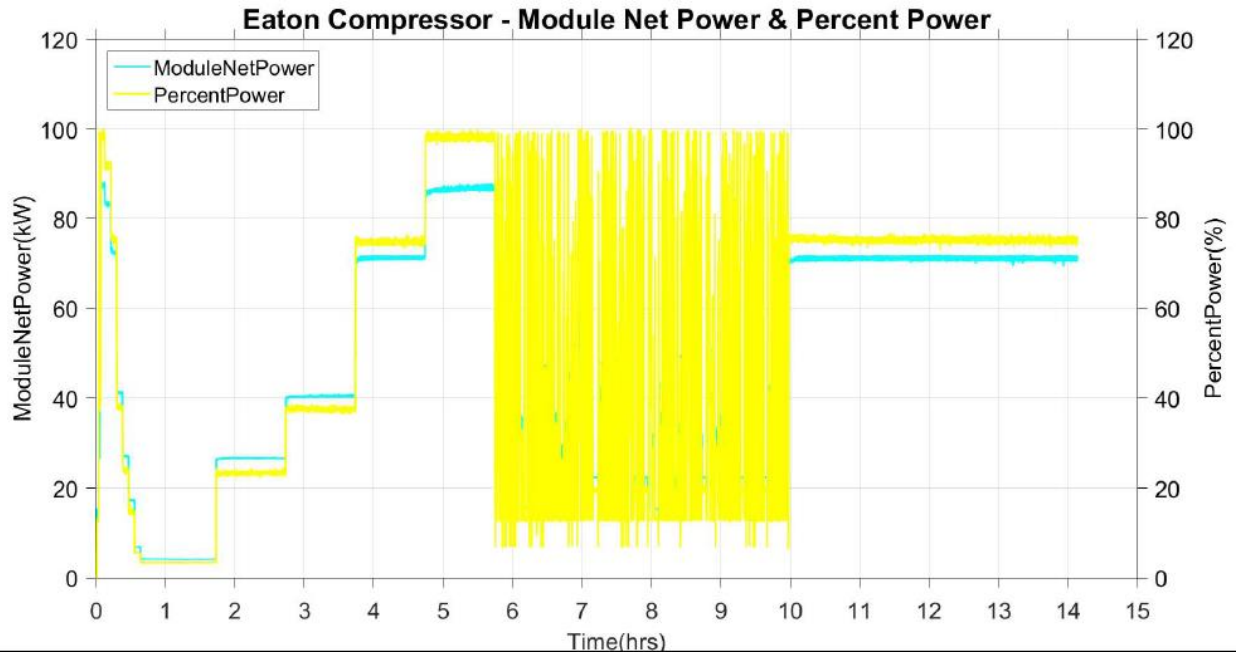

Figure 90. Configuration 1 Testing – Module Net Power and Percent Power

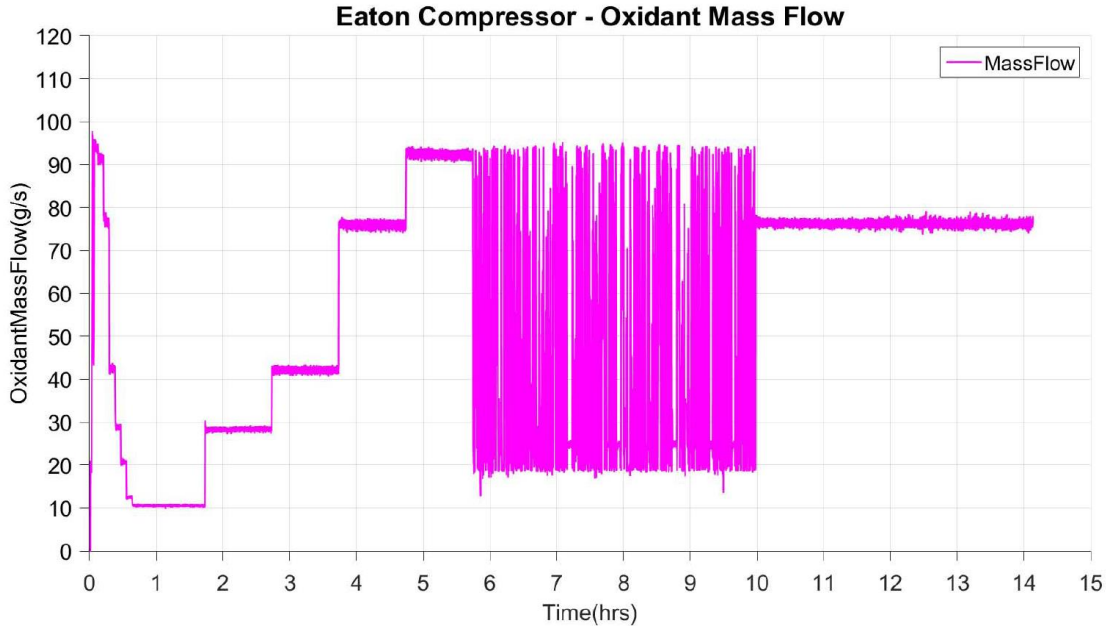

Figure 91. Configuration 1 Testing - Oxidant Mass Flow

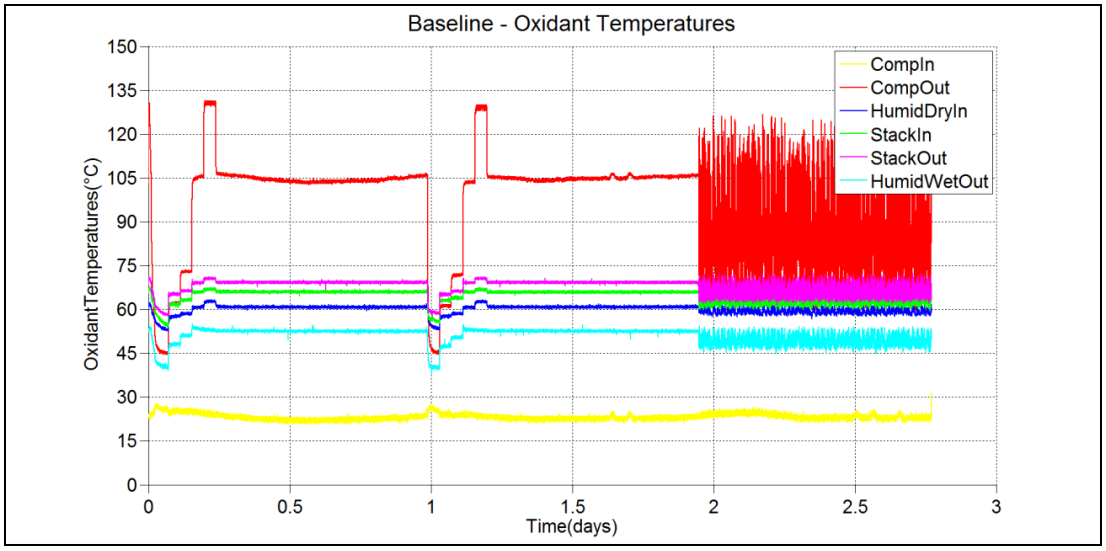

Figure 92. Baseline Testing - Oxidant Temperatures

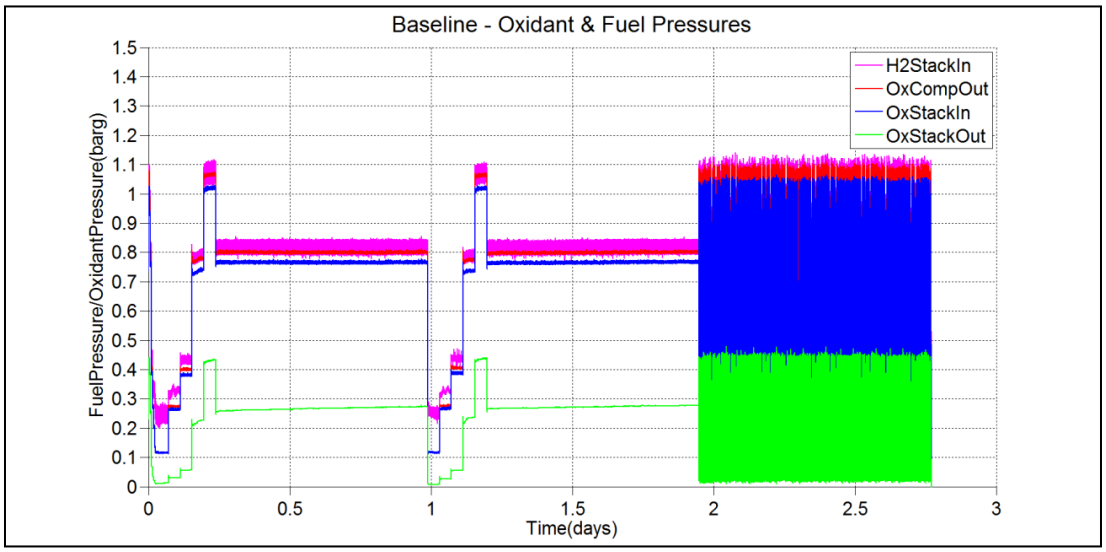

Figure 93. Baseline Testing - Oxidant and Fuel Pressures

Additionally, the compressor current and power were logged, as shown in Figure 94 and Figure 95. The data collected can be used to directly compare the performance of the existing system with Eaton's Air Management System.

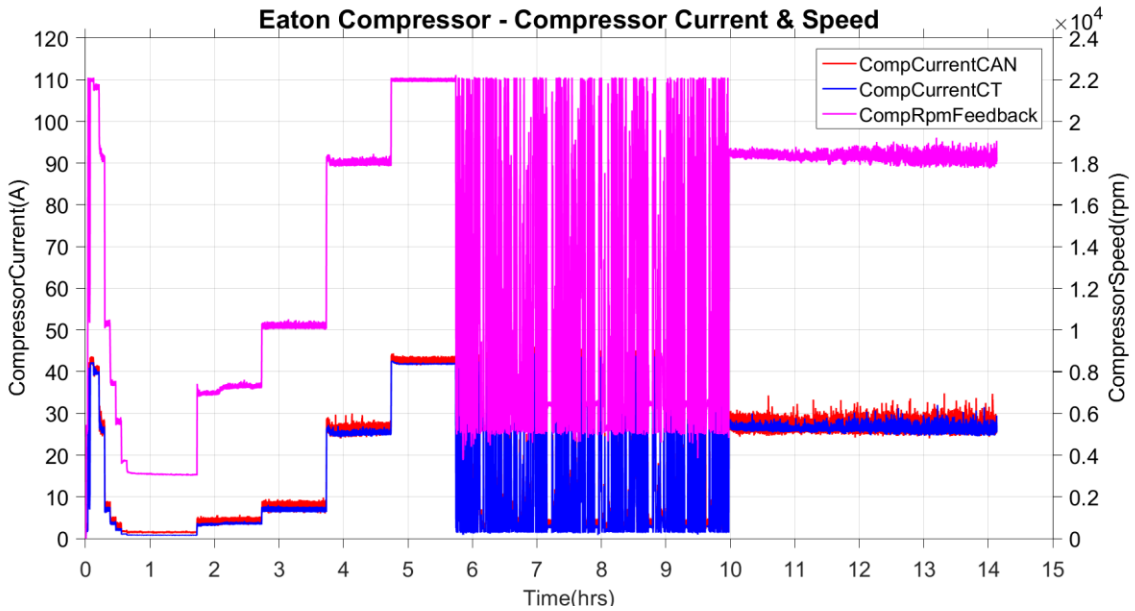

Figure 94. Configuration 1 Testing – Compressor Current and Speed

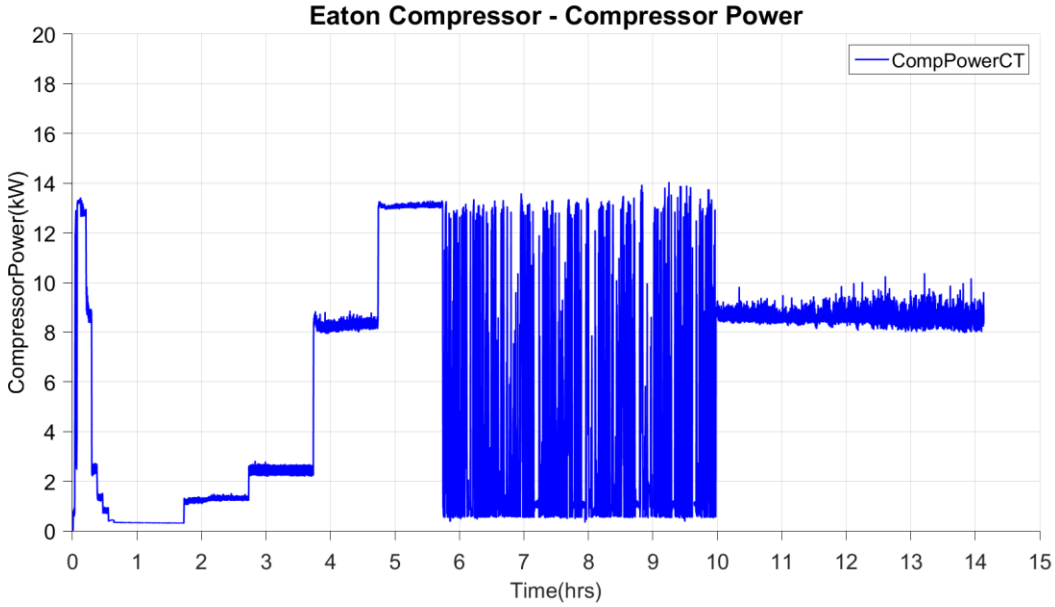

Figure 95. Configuration 1 Testing – Compressor Power

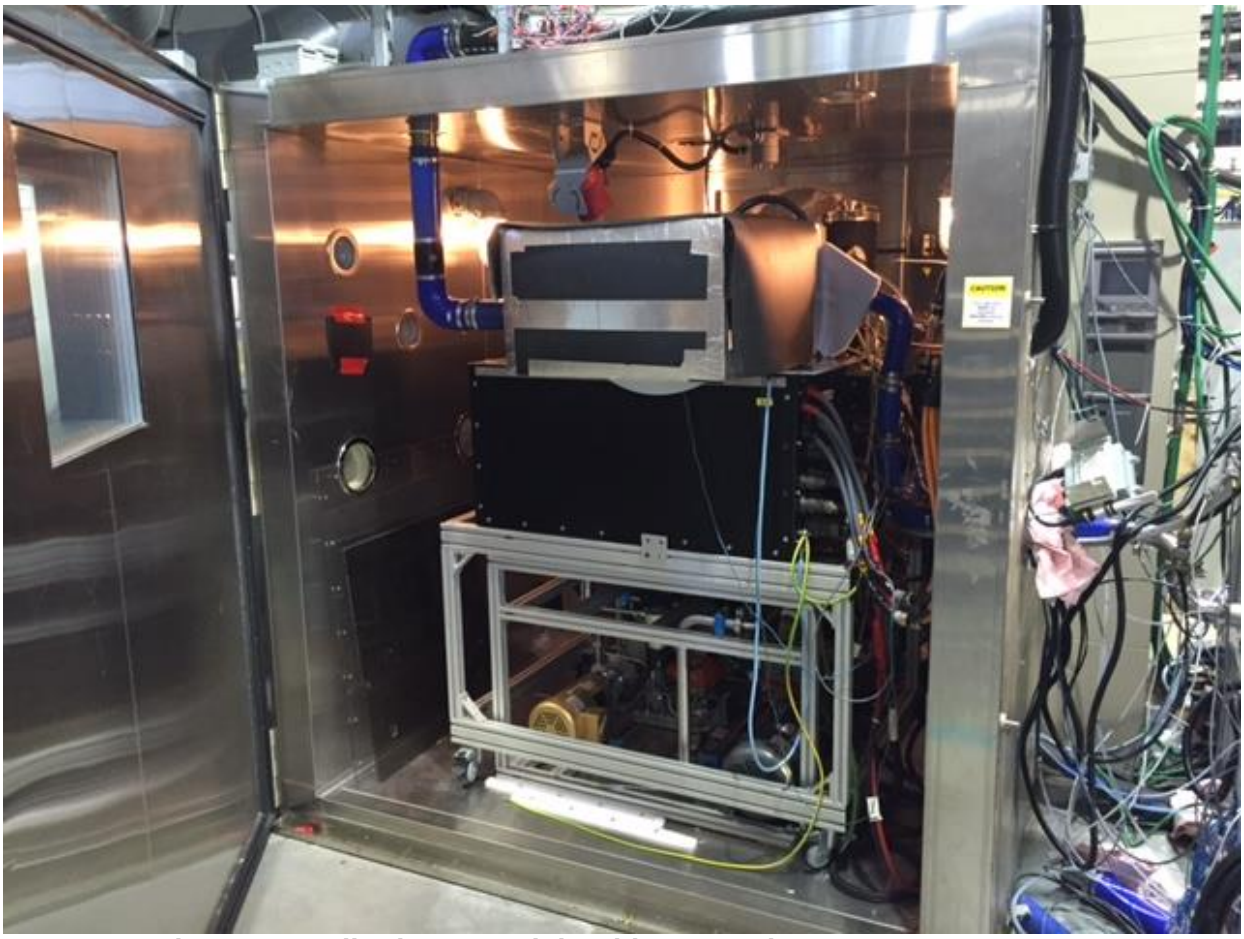

Figure 96: Ballard HD7 Module with Eaton Air Management System

Using data from the first completed cycle the performance of the Eaton compressor with the Ballard HD7 FCM had an efficiency of 47.4% LHV H2 at the steady state operating point of 240A Fuel Cell current, slightly less than the Ballard incumbent system.

3.7.4.4 Eaton Compressor with Expander in Configuration 2

The proposed setup for configuration 2 is shown in Figure 97 below. Testing with the Eaton Compressor/Expander was limited to non-business hours due to the excessive noise of the unit in operation thus severely limiting operations on the Ballard test bench. Due to time constraints with test station availability and there was limited benefit expected in this setup the testing was abandoned.

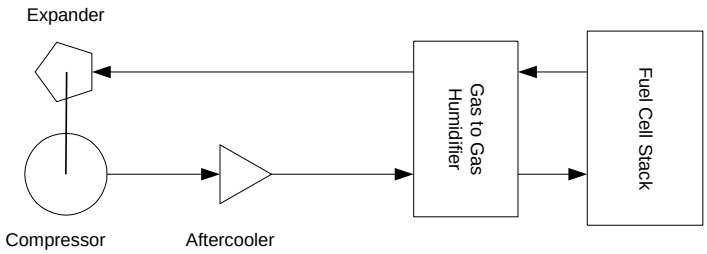

Figure 97: Configuration 2 Test Setup

3.7.4.5 Eaton Compressor with Expander in Configuration 3

The HD7 system operated using the upgraded compressor air system in position 3, however was only able to operate up to 180A during the initial run and shutdown from a fuel cell alarm due to air pressure being outside of specification. A second attempt was made with the addition of a smaller bypass valve around the expander to prevent excessive pressure drop that was the suspected cause of inoperability for the first trial. Unfortunately this too was unsuccessful. The unit was able to operate up to 120A followed by a 60A steady state point before shutting down and not able to follow the test protocol as designed.

Figure 98 below shows the test setup for configuration 3

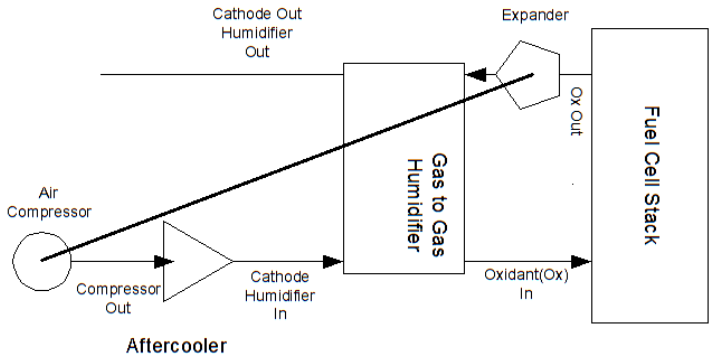

Figure 98: Configuration 3 test set-up

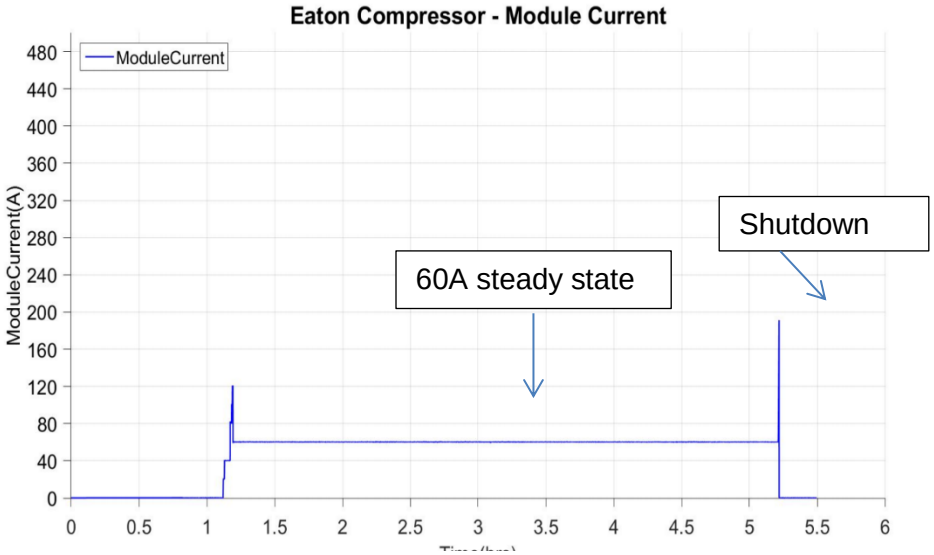

Figure 99: Configuration 3 Testing - Module Current

During testing, a data acquisition system logged process parameters internal to the module. These include stack-specific parameters, including voltage and current, as well as air system-specific parameters, including flows, temperatures and pressures measured throughout the air

system. Figure 100 through Figure 103 provide a graphical representation of a sample of the data collected.

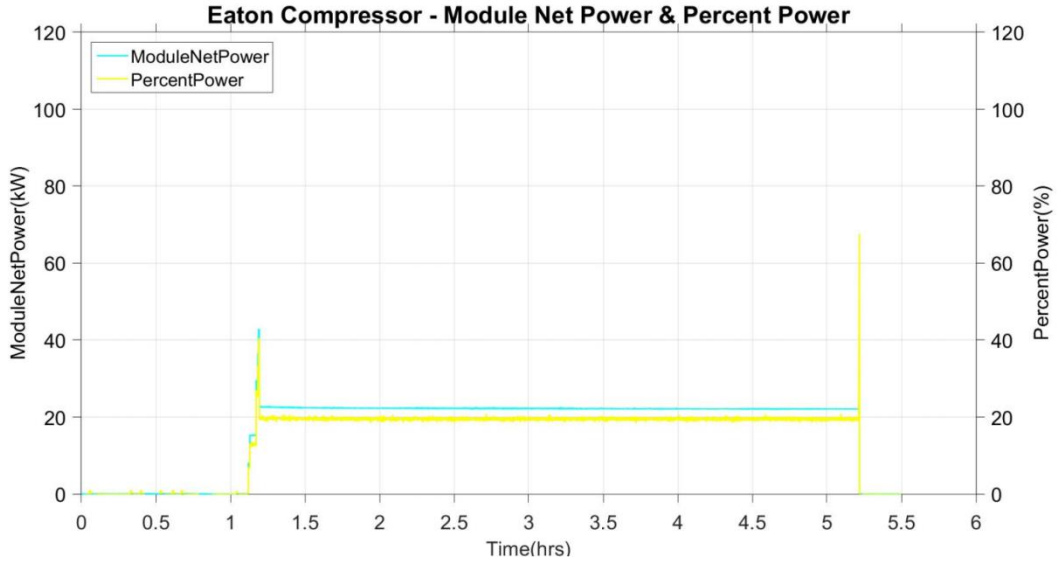

Figure 100: Configuration 3 Testing – Module Net Power and Percent Power

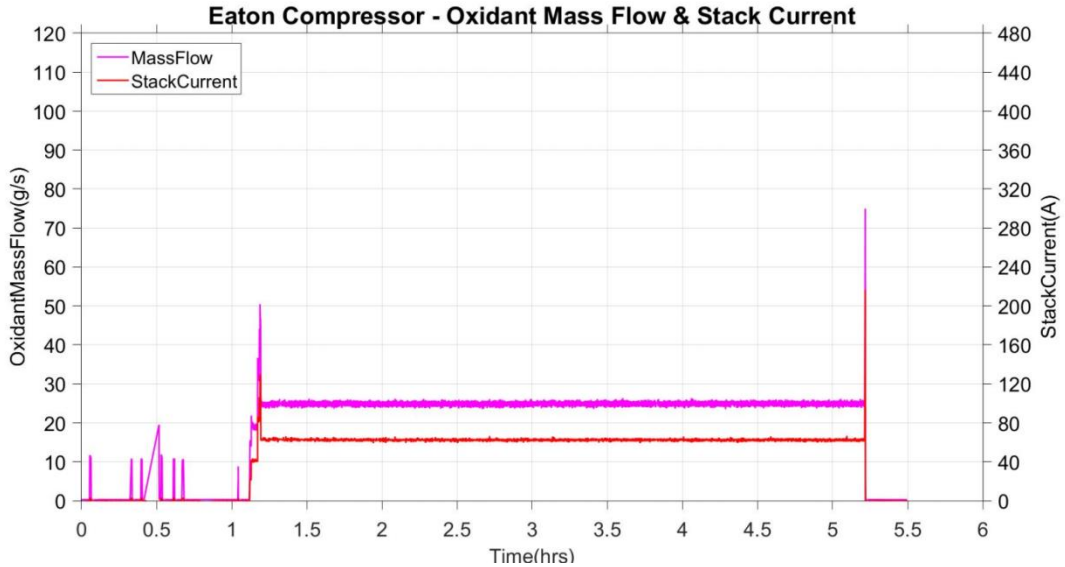

Figure 101: Configuration 3 Testing - Oxidant Mass Flow

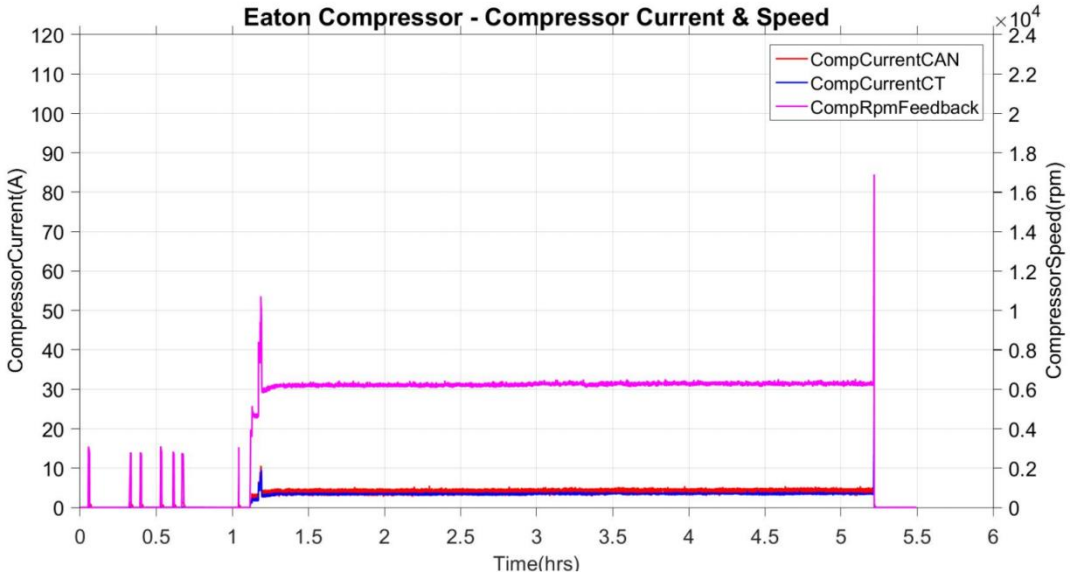

Figure 102: Configuration 3 Testing – Compressor Current and Speed

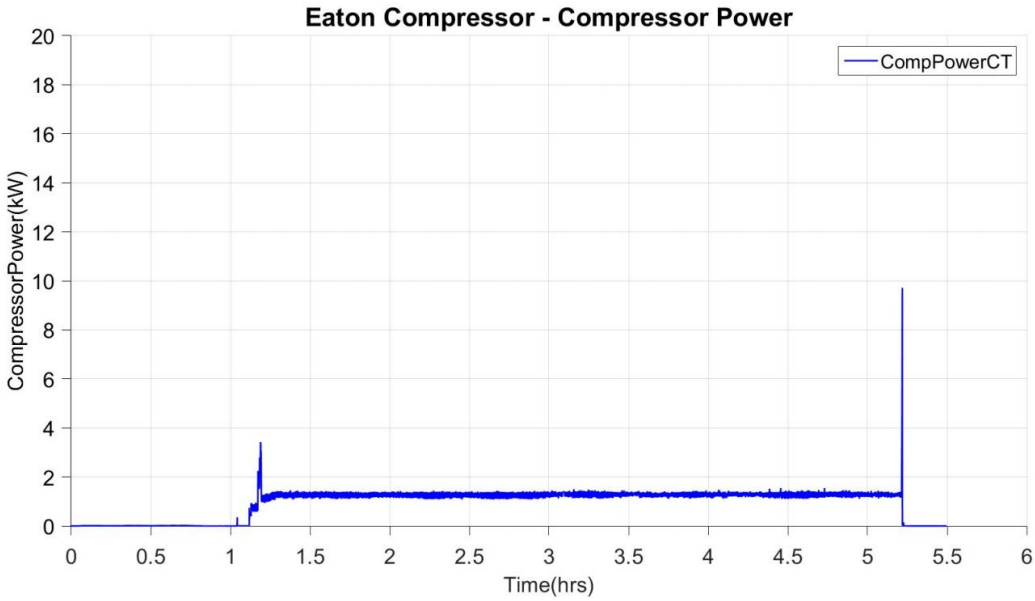

Figure 103: Configuration 3 Testing – Compressor Power

3.7.4.6 Water Injection Testing

Due to Ballard test station availability issues only the initial water injection tests were able to be performed providing proof of concept for humidification and temperature reduction of the compressor air outlet temperature.

Compressor RPM	Flow (g/s)	Pressure (barg)	temperature (°C)	Dew Point (°C)	H2O injected (ml/min)
11000	50.1	0.49	88.1	22.8	0
11000	51	0.49	42.4	42.1	500
11000	50.5	0.49	42.3	42.1	250

Table 9: Water Injection Results

3.7.5 *Conclusions*

Due to the low pressure of the fuel cell exhaust there does not seem to be a benefit for the Eaton compressor/expander combination and results in a less efficient air delivery system.

These results suggest the Eaton compressor with expander is not a viable product for the HD7 fuel cell module in the current configuration. The current technical direction is to operate PEM fuel cells at lower pressures thus reducing likelihood of expander technology being economically feasible in this application.

4 PRODUCTS DEVELOPED/TECHNOLOGY TRANSFER ACTIVITIES

Dale Stretch presented at the following conferences over the course of the program:

- 2013 DOE Hydrogen and Fuel Cells Program Review on May 14, 2013.
- U.S. DRIVE Technical Meetings - Fuel Cell Tech Team (FCTT), February 11, 2014
- 2014 DOE Hydrogen and Fuel Cells Program Review on June 14, 2014.
- U.S. DRIVE Technical Meetings - Fuel Cell Tech Team (FCTT), February 11, 2015
- 2015 DOE Hydrogen and Fuel Cells Merit Review on June 10, 2015.

No patents have been applied for under this program.

5 COMPUTER MODELING DETAILS

Computer modeling details can be found in Section 3.1: Analytical Development of the Compressor & Expander using CFD Modeling.